









FILAMENTS OF THE SLIME MOLD COSMIC WEB AND HOW THEY AFFECT GALAXY EVOLUTION

FARHANUL HASAN ¹, JOSEPH N. BURCHETT ¹, DOUGLAS HELLINGER,² OSKAR ELEK ³, DAISUKE NAGAI ⁴,
S. M. FABER ⁵, JOEL R. PRIMACK ², DAVID C. KOO ⁵, NIR MANDELKER ⁶ AND JOANNA WOO⁷

¹Department of Astronomy, New Mexico State University, Las Cruces, NM 88003, USA

²Department of Physics, University of California, Santa Cruz, CA 95064, USA

³Department of Computational Media, University of California, 1156 High Street, Santa Cruz, CA 95064, USA

⁴Department of Physics, Yale University, New Haven, CT 06520, USA

⁵University of California Observatories and Department of Astronomy and Astrophysics,
University of California, Santa Cruz, 1156 High Street, Santa Cruz, CA 95064, USA

⁶Centre for Astrophysics and Planetary Science, Racah Institute of Physics, The Hebrew University, Jerusalem 91904, Israel

⁷Department of Physics, Simon Fraser University, 8888 University Drive, Burnaby, BC, V5A 1S6, Canada

ABSTRACT

We present a novel method for identifying cosmic web filaments using the IllustrisTNG (TNG100) cosmological simulations and investigate the impact of filaments on galaxies. We compare the use of cosmic density field estimates from the Delaunay Tessellation Field Estimator (DTFE) and the Monte Carlo Physarum Machine (MCPM), which is inspired by the *slime mold* organism, in the DISPERSE structure identification framework. The MCPM-based reconstruction identifies filaments with higher fidelity, finding more low-prominence/diffuse filaments and better tracing the true underlying matter distribution than the DTFE-based reconstruction. Using our new filament catalogs, we find that most galaxies are located within 1.5–2.5 Mpc of a filamentary spine, with little change in the median specific star formation rate and the median galactic gas fraction with distance to the nearest filament. Instead, we introduce the filament line density, Σ_{fil} (MCPM), as the total MCPM overdensity per unit length of a local filament segment, and find that this parameter is a superior predictor of galactic gas supply and quenching. Our results indicate that most galaxies are quenched and gas-poor near high-line density filaments at $z \leq 1$. At $z = 0$, quenching in $\log(M_*/M_\odot) \gtrsim 10.5$ galaxies is mainly driven by mass, while lower-mass galaxies are significantly affected by the filament line density. In high-line density filaments, satellites are strongly quenched, whereas centrals have reduced star formation, but not gas fraction, at $z \leq 0.5$. We discuss the prospect of applying our new filament identification method to galaxy surveys with SDSS, DESI, Subaru PFS, etc. to elucidate the effect of large-scale structure on galaxy formation.

1. INTRODUCTION

Understanding how galaxies form and change over time is a major challenge in astrophysics. The mass of a galaxy plays a crucial role in determining its observable physical properties, as it determines the strength of internal processes such as supernovae (SNe) and active galactic nucleus (AGN) feedback (e.g., Kauffmann et al. 2004; Baldry et al. 2006; Faber et al. 2007; Peng et al. 2010; Ilbert et al. 2013; Schawinski et al. 2014). Moreover, the environment surrounding galaxies is also a significant factor in shaping their physical properties, highlighting the importance of the interaction between a galaxy and its surroundings in the process of evolution (e.g., Dressler 1980; Balogh et al. 1999; Elbaz et al. 2007; Darvish et al. 2016; Kraljic et al. 2018; Sobral et al. 2022).

Identifying the salient “environmental” indicator of a galaxy is a task that has been approached differently in various studies. Dark matter (DM) halos in which galaxies form

play a critical role in shaping galactic properties (e.g., Yang et al. 2012; Behroozi et al. 2013; Zu & Mandelbaum 2016; Wechsler & Tinker 2018; Scholz-Díaz et al. 2023). The environmental effects are particularly pronounced in satellite galaxies in massive clusters and groups (Moore et al. 1996; Poggianti et al. 2006; De Lucia et al. 2007; Tonnesen et al. 2007; Brown et al. 2017; Zavala et al. 2019). Therefore, it is expected that the properties and evolution of galaxies depend on local environments typically characterized by the galaxy overdensity or the distance to the N^{th} nearest neighbor (or variants thereof; e.g., Blanton et al. 2005; Peng et al. 2012; Woo et al. 2013; Darvish et al. 2014; Davidzon et al. 2016; Moutard et al. 2018).

Galaxy evolution can be analyzed in the context of the universe’s large-scale structure, known as the “cosmic web.” This structure consists of an interconnected network of filaments, which are bridges of intergalactic matter, and nodes, which are dense intersections of filaments where the cosmic density distribution is highest (e.g., White et al. 1987; Bond et al. 1996; Springel et al. 2005; Sousbie et al. 2011; Cautun et al. 2014; Martizzi et al. 2019). Galaxies are usu-

ally found within these structures. The cosmic web structure has been inferred from galaxy redshift surveys for several decades (e.g., de Lapparent et al. 1986; Geller & Huchra 1989; Colless et al. 2001; Strauss et al. 2002; Lilly et al. 2007; Driver et al. 2011; Huchra et al. 2012; Bryant et al. 2015; Laigle et al. 2016). Although the nodes of the cosmic web can be easily identified by the location of the most massive halos, such as clusters and groups (e.g., Kaiser 1984; Sheth & Tormen 2004; Walker et al. 2019; Kuchner et al. 2020; Cohn 2022), identifying the filamentary structure is much more challenging.

Identifying the filaments of the cosmic web from a sparse distribution of galaxies, commonly known as cosmic web “reconstruction,” is a challenging task. Various techniques have been proposed to achieve this goal, including graph theory and percolation-based methods, such as minimal spanning trees (e.g., Alpaslan et al. 2014), stochastic methods, such as the Bisous point process model (e.g., Tempel et al. 2014), Hessian-based methods exploiting the geometry of local density, tidal, or velocity shear fields (e.g., Cautun et al. 2013), phase-space methods based on the dynamics of the cosmic web (e.g., Falck et al. 2012), and topological methods that exploit the connectivity and topology of space, such as SPINWEB (Aragón-Calvo et al. 2010) and DISPERSE (Sousbie 2011; Sousbie et al. 2011). For a comprehensive comparison of these methods and the resulting cosmic web reconstructions, refer to Libeskind et al. (2018). According to the authors, there is general agreement between the spatial and statistical distribution of the identified structures. Voids occupy most of the volume, and clusters live in nodes. However, there are significant disagreements in some cases, such as the mass/volume fractions in filaments. These disagreements can lead to different conclusions being drawn on the effect of large-scale structure on galaxy formation (Rost et al. 2020).

Recent advances in cosmic web reconstruction techniques have enabled us to study the impact of filaments on various aspects of galaxy formation. These studies have explored the effect of filaments on quenching (e.g., Kuutma et al. 2017; Kraljic et al. 2018; Laigle et al. 2018; Alam et al. 2019; Singh et al. 2020; Xu et al. 2020; Winkel et al. 2021; Malavasi et al. 2022; Bulichi et al. 2023; Hasan et al. 2023), gas supply (e.g., Moorman et al. 2014; Stark et al. 2016; Janowiecki et al. 2017; Kleiner et al. 2017; Crone Odekon et al. 2018; Song et al. 2021; Galárraga-Espinosa et al. 2022; Rosas-Guevara et al. 2022; Zhu et al. 2022), and alignment between galaxy spin and filament direction (e.g., Codis et al. 2012, 2018; Tempel et al. 2013; Dubois et al. 2014; Ganeshaiyah Veena et al. 2019; Pandya et al. 2019; Kraljic et al. 2019, 2021; Blue Bird et al. 2020; Welker et al. 2020; Tudorache et al. 2022; Zhang et al. 2023), both in observations and simulations. However, the methods used to identify filaments vary widely, and the conclusions drawn regarding the physical effect of filaments on galaxy formation phenomena are often divergent. For example, while some studies suggest a suppression of gas (e.g., Crone Odekon et al. 2018; Zhu et al. 2022; Hasan et al. 2023) and star formation (e.g., Alpaslan

et al. 2014; Kraljic et al. 2018; Malavasi et al. 2022) near filaments, others report an increase in gas supply and/or star formation (e.g., Kleiner et al. 2017; Vulcani et al. 2019; Kotecha et al. 2022).

This work follows from Hasan et al. (2023, hereafter Paper I), who use the aforementioned DISPERSE framework to reconstruct the cosmic web in all snapshots of the IllustrisTNG cosmological simulations (Pillepich et al. 2018; Nelson et al. 2018, 2019) between redshifts $z = 0$ and $z = 5$. They examined the effect of proximity to the nearest cosmic web filaments and nodes on the quenching and gas supply of galaxies at different masses and epochs. The study revealed that, at earlier times ($z \gtrsim 2$), the average star formation activity of galaxies is not affected by the proximity to the cosmic web. However, at later times, galaxies are more likely to quench closer to nodes and filaments. This trend is particularly noticeable in low-mass galaxies ($8 \leq \log(M_*/M_\odot) < 9$) and satellites of all masses. The study also found that the primary reason behind these effects is the decline in galactic gas supply is directly with cosmic web proximity.

In this paper, we present a new technique for reconstructing the cosmic web from galaxy catalogs. We compare the impact of the resulting structure on galaxy evolution between our method and the one used in Paper I. Our approach uses a novel model called the Monte Carlo Physarum Machine (MCPM; Burchett et al. 2020; Elek et al. 2021, 2022) to estimate the cosmic density field. MCPM is inspired by the feeding habits of the biological organism *Physarum polycephalum* or *slime mold*, which is known to generate highly efficient interconnected networks when searching for food. This behavior has been often used to model spatial problems in various disciplines, from neuroscience to civil engineering (see, e.g., the review from Adamatzky 2010).

The MCPM algorithm takes a catalog of point sources as input, which in this paper is a catalog of galaxies with a stellar mass of $\log(M_*/M_\odot) \geq 8$. It then infers a continuous cosmic matter density field at every location in the input volume, *even in underdense regions far from galaxies*. This is what makes the MCPM density field unique and sets it apart from other methods, such as the Delaunay Tessellation Field Estimator (DTFE; Schaap & van de Weygaert 2000; van de Weygaert & Schaap 2009), which is integrated into DISPERSE and only provides density field estimates around the location of galaxies. The MCPM model has been applied to analyze observational galaxy catalogs (Burchett et al. 2020; Wilde et al. 2023) and fast radio burst data (Simha et al. 2020). It has successfully recovered the density structure of the cosmic web and provided crucial insights into the intergalactic universe. Among other findings, the MCPM density field can trace neutral hydrogen gas (Burchett et al. 2020) and hot ionized gas (Simha et al. 2020) in the cosmic web.

In this work, we replace the DTFE density field with the MCPM density field in DISPERSE to reconstruct the cosmic web structure in IllustrisTNG (TNG100). We carry out this task on six snapshots ranging from $z = 0$ to $z = 4$. Our approach has significantly improved the filament identification scheme in DISPERSE, widely used as a cosmic web

reconstruction tool. We highlight the effect of cosmic web environment on the quenching and gas supply of galaxies using filaments from our new method. This finding will be invaluable for understanding the interplay between galaxies and large-scale structures, especially as our method is applicable to observational galaxy catalogs.

The paper is organized as follows. In Section 2, we describe the simulation data and the methods used to reconstruct the cosmic web. We also compare two different methods. In Section 3, we present our findings on how galactic star formation and the gas fraction depend on cosmic web environments. We discuss our results in Section 4, and conclude the paper in Section 5. We adopt the *Planck 2015* cosmology (Planck Collaboration et al. 2016), as in Paper I, with $H_0 = 67.74 \text{ km s}^{-1} \text{ Mpc}^{-1}$, $\Omega_{M,0} = 0.3089$, and $\Omega_{\Lambda,0} = 0.6911$. Unless otherwise stated, all distances and lengths are in comoving units.

2. DATA AND METHODS OF COSMIC WEB RECONSTRUCTION

2.1. TNG Simulations

We analyzed the outputs from the IllustrisTNG magneto-hydrodynamical cosmological simulations (Pillepich et al. 2018; Nelson et al. 2018, 2019), which used the AREPO moving-mesh hydrodynamics code (Springel 2010) to simulate the evolution of gas, stars, dark matter, and black holes from the early universe ($z = 127$) to the present day ($z = 0$). The highest resolution run of the TNG100 simulation, TNG100-1, was used, which has a box size of approximately 110.7 comoving Mpc per side, a minimum baryonic particle mass of $\sim 1.4 \times 10^6 M_\odot$, and cosmology based on *Planck 2015* (Planck Collaboration et al. 2016). This is similar to the approach used in Paper I.

We obtain galaxy data for all 100 snapshots of the TNG100-1 simulation (hereafter TNG) from the online data repository¹, as presented first in (Nelson et al. 2019). In each snapshot, we construct ‘‘Group’’ catalogs by using the friends-of-friends (FoF) substructure identification algorithm, and ‘‘subhalo’’ catalogs are constructed using the SUBFIND algorithm (Springel et al. 2001; Dolag et al. 2009). The ‘‘subhalo’’ catalogs contain gravitationally bound objects within a FoF group, while the ‘‘Group’’ catalogs identify halos. Hereafter, we refer to groups as halos, and subhalos as galaxies.

Similarly to Paper I, we set a minimum stellar mass of $10^8 M_\odot$ and DM halo mass of $10^9 M_\odot$ within a sphere of mean density 200 times the critical density of the Universe in each snapshot. This ensures that the galaxies are adequately resolved, having at least around 100 stellar particles, and correspondingly, their host halos have around 100 DM particles. We then extracted the following data from the galaxy and halo catalogs at each snapshot from $z = 5$ to $z = 0$: the galaxy’s comoving position, its star formation rate (SFR), its stellar mass (M_*), its halo mass ($M_{200,c}$), its halo virial radius ($R_{200,c}$; comoving radius where $M_{200,c}$ is calculated),

¹ <http://www.tng-project.org/data/>

the mass of all gas gravitationally bound to a subhalo (M_{gas}), and synthetic stellar magnitudes in the SDSS g, r, i, z bands (Stoughton et al. 2002). For more information on the photometric bands, including a comprehensive dust attenuation modeling, see Nelson et al. (2018).

2.2. DISPERSE Cosmic Web Reconstruction

In this work, we use the Discrete Persistent Structures Extractor (DISPERSE) algorithm² (Sousbie 2011; Sousbie et al. 2011) to reconstruct the cosmic web structure from input galaxy catalogs. There are three main steps in a typical DISPERSE workflow for 3D input data (the steps are almost identical for 2D data).

1. Apply point-set inputs – in our case, catalog of galaxies with $\log(M_*/M_\odot) \geq 8$ – to the *delaunay_3d* program. In this step, a technique called the Delaunay Tessellation Field Estimator (DTFE; Schaap & van de Weygaert 2000) is used to tessellate the entire input volume into tetrahedrons, with the positions of individual galaxies as vertices. The output is a 3D network file, containing the density field estimate at the *locations of the vertices* (i.e., galaxy positions).
2. Apply the 3D density field estimate to *mse*, the main program in DISPERSE. Here, the gradients of the density field are computed, and critical points are determined where the gradient is zero, corresponding to the voids (minima), saddle points, and nodes (maxima) of the density field. Filaments are defined as segments connecting maxima to saddle points following ridges of the density field. The output of *mse* is a so-called ND skeleton file, which contains the filamentary network described by a list of critical points, segments that make up filaments, and filaments that originate and lead to maxima.
3. The final step is to apply the ND skeleton output to *skelconv* so that the output can be converted to a non-binary format that humans can read.

We first reconstruct the cosmic web in each TNG snapshot from $z = 0$ to $z = 5$ following these steps above. In addition to this nominal procedure, we make several choices to improve the reconstruction. In step 1, i.e., during the DTFE density field estimation, the density field at the position of each vertex is smoothed by averaging it with that of its two nearest neighbors to minimize contamination by noise and detection of spurious features on a small scale (see, e.g., Malavasi et al. 2022). In step 3, we apply smoothing to the position of the segments of the filamentary skeleton by averaging the initial positions of the extrema of a segment with those of the contiguous segments. Here, the critical points are fixed, and the coordinates of each point along a filament are averaged with that of its two neighbors so that sharp and/or unphysical shapes (caused by shot noise) are not seen in fila-

² <http://www2.iap.fr/users/sousbie/web/html/indexd41d.html>

ment segments. The impact of smoothing is discussed more in section 2.4.

Persistence is the key parameter used by DISPERSE to determine the significance of topologically identified structures. DISPERSE identifies topologically significant pairs of critical points, also known as persistence pairs, and associates each pair with a persistence value. This value is defined as the density ratio at the two critical points. The persistence value measures the robustness of the identified topological structure to local fluctuations in the density field due to shot noise in the input data. A higher persistence structure is more significant and robust than a lower one. In practice, the persistence level can be set directly in *mse* using the option “-cut” in terms of a persistence value or using the option “-nsig” in terms of the probability that a given structure appears in a random field. In Section 2.4, we discuss the choice of persistence value when using different methods.

2.3. The MCPM model and Application to TNG

The MCPM algorithm was first introduced in a paper by Burchett et al. (2020). It is an agent-based generative model designed to emulate the growth of the unicellular organism *Physarum polycephalum*, commonly known as *slime mold*. This organism is known to explore its environment for food sources and shape itself into highly intricate networks to connect them. Scores of researchers across various fields like computational science, biology, design engineering, etc. have used this behavior as inspiration for solving a wide range of spatial problems, such as navigating labyrinths (Nakagaki et al. 2000), designing transportation networks (Tero et al. 2010), and understanding human cognitive patterns and creativity (Adamatzky et al. 2013).

The MCPM algorithm is a modification of the model of Jones (2010), who proposed a virtual *Physarum* machine with a simulated slime mold network. Similarly to their work, MCPM models the slime mold as discrete particle-like “agents” that swarm toward “food sources”. The food sources, i.e., the input data, emit a continuous lattice of markers that agents are drawn towards, while the agents themselves emit a marker of the path they trace. The optimal transport network generated by this process results from the feedback loop between the agents and the markers of the food sources.

The MCPM algorithm is an effective method for tracing out a density field from discrete input data. The input data are usually positions of galaxies or halos, but it can also be other data types such as positions of DM or gas particles in simulations. The algorithm uses millions of slime mold agents that act as virtual agents to find food sources in the input data. The agents deposit markers that are proportional to the weight of each input data point, typically stellar or halo mass. The agents are guided by the markers and have a higher probability of moving towards regions with higher deposit values. We refer the readers to Burchett et al. (2020), Elek et al. (2021), and Elek et al. (2022) for more details.

Although the Jones (2010) model was designed so that agents follow the direction of maximum deposit, this would

generate extremely condensed and less inter-connected filamentary networks than are observed and expected from theory, therefore not capturing the true complexity of the multi-scale structures of the cosmic web (Burchett et al. 2020; Elek et al. 2022). Instead, in MCPM, the extracted 3D network is a probability density of the cosmic matter distribution, enabled by three different probability distributions that determine the direction and distance an agent moves relative to its initial state at each run iteration. These require the agents to navigate towards large pools of deposits preferentially, connecting the galaxies/halos (via input data deposits) to each other and reinforcing existing pathways (via agent deposits), as well as ensuring that angular momentum is conserved and agents do not end up stuck in local deposit pools. Elek et al. (2022) showed that MCPM misses less than $\sim 0.1\%$ of the input data points, meaning that virtually all of the input galaxies are reliably contained by the reconstruction.

The main output of MCPM is a continuous 3D trace field. This field is the time-averaged equilibrium density field of the agents, which is created by superposing all individual agent trajectories. This field can be interpreted as the total probability of the agents’ distribution marginalized over all possible geometric configurations within the input domain. The trace density field is an excellent proxy of the cosmic matter density field, as long as the trace density at each 3D location is mapped to the corresponding physical DM mass density. In Burchett et al. (2020), such a mapping between the trace density of MCPM and the DM overdensity was performed for the large Bolshoi-Planck (BP) N body cosmological simulation (Klypin et al. 2016) at $z = 0$. They found a strong correlation between the trace density and the DM overdensity at higher trace densities, but a roughly flat DM overdensity for very low trace densities. This is due to the much larger dynamic range of the MCPM trace values than the matter density values from BP. In Section 2.4, we compare the mapping between the overdensity of MCPM and the overdensity of DM particles in TNG100 at $z = 0$. We show that the MCPM overdensity maps very well to the physical cosmic mass overdensity for virtually all overdensities.

MCPM data fitting is a semi-supervised process aided by a graphical data visualization component, through the original visualization software POLYPHORM (Elek et al. 2021), and the recent successor, POLYPHY³. These allow a user to tune the model’s hyperparameters in real-time to obtain the best possible fit, which optimizes a fitness/objective function that determines the level of “connectedness” of a fit (see Elek et al. (2022) for details). The interactive visualization ensures that the reconstruction produces a filamentary network and not a series of disconnected islands. We recognize that the ideal fitting procedure would rigorously optimize the fitness function against the reference TNG DM density field. While beyond the scope of this work, we aim to address this issue in the future to obtain a precise mathematical formulation of the fitness function and transform MCPM from a semi-supervised to a fully automated reconstruction tool.

³ <https://polyphy.io/>

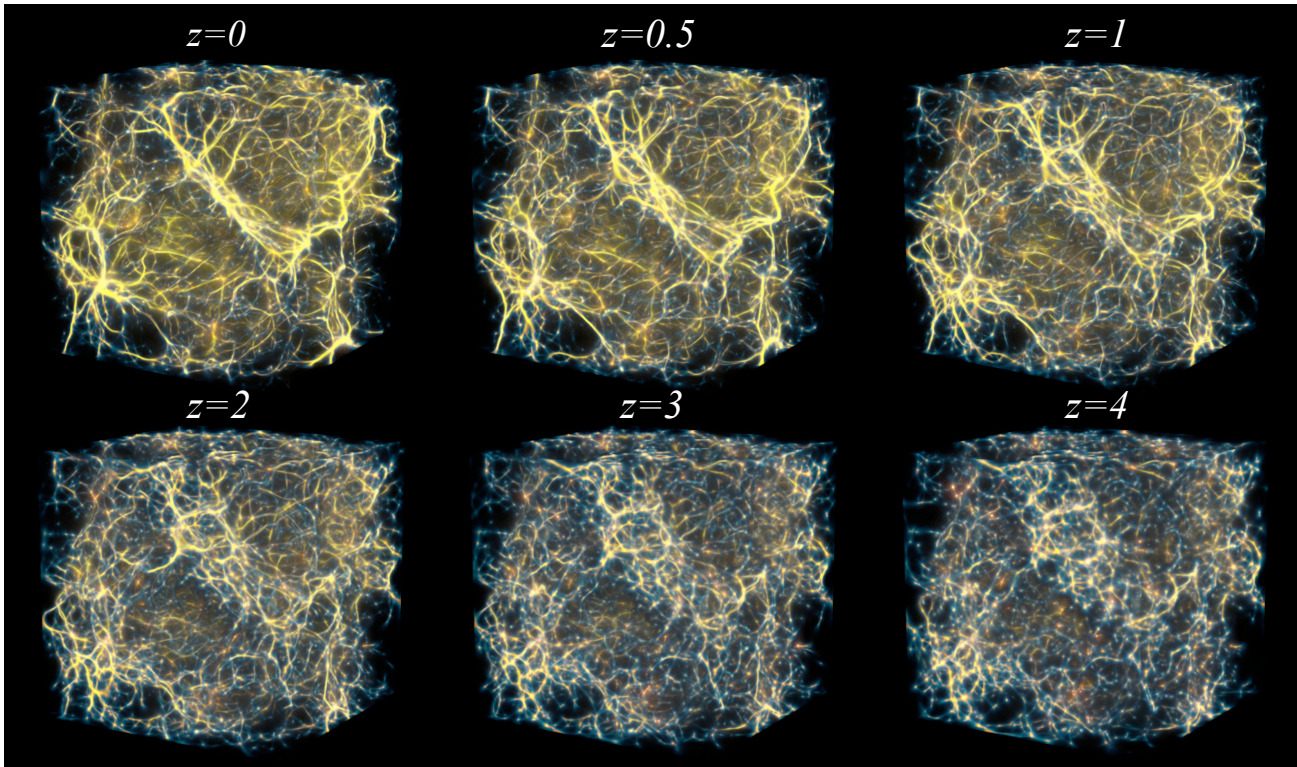


Figure 1. The MPCM trace density field output for TNG100 at redshifts $z = 0, 0.5, 1, 2, 3,$ and 4 . In each cube, input galaxies ($\log(M_*/M_\odot) \geq 8$) are represented by glowing white dots, and the density field is represented by the green-to-yellow colorbar (yellow are regions of higher density). The following *sharpness* values were adopted: $z = 0$: 2.51; $z = 0.5$: 2.18; $z = 1$: 2.0, $z = 2$: 1.8; $z = 3$: 1.61; $z = 4$: 1.42. Figures were rendered with the POLYPHY visualization tool for MPCM.

Based on our previous experiments, we have observed that the most important hyperparameter in the optimization process is the “sharpness” parameter. This parameter measures the geometric definition of the output density field. A lower “sharpness” value will produce more interconnected and “fuzzier” filaments, while higher “sharpness” values will result in cylindrical or tubular filaments that are poorly connected. After testing, we found that a “sharpness” parameter of approximately 2.5 is optimal for fitting the MPCM to halos in the BP simulations at a redshift of 0. This produces a linear mapping between the trace density and the DM density. However, we expect the cosmic web at earlier times to be less condensed and fuzzier at higher redshifts (e.g., [Cautun et al. 2014](#); [Martizzi et al. 2019](#)). As such, the *sharpness* parameter must decrease with increasing redshift. We found that decreasing the *sharpness* parameter from ~ 2.5 at $z = 0$ to ~ 1.4 at $z = 4$ produced the most optimal fitness function, while also visually agreeing with the known density distribution of matter in TNG100.

We reconstruct the MPCM cosmic matter density field in TNG100 at redshifts $z = 0, 0.5, 1, 2, 3,$ and 4 ; the outputs of each are presented in Figure 1. To do this, each fit used 5 million agents, more than 100 times the number of agents as data points (galaxies with $\log(M_*/M_\odot) \geq 8$). The grid was 512 voxels per ~ 110.7 Mpc side, resulting in a grid resolution of ≈ 0.25 Mpc. We stress that varying most of the hyperpa-

rameters in the fits, including *sharpness*, does not affect the qualitative aspects of the reconstruction or the quantitative analysis presented later in the paper. Additionally, previous studies have demonstrated that cosmic density reconstruction is highly robust to changes in the sparseness (number density) of input data and data volume.

2.4. Applying the MPCM Density Field in DISPERSE

MPCM produces a continuous estimate of the 3D density field at each pixel of the reconstructed volume. This is a significantly more informative description of the cosmic density field as it provides a density estimate at $> 10^8$ spatial locations of the TNG100 volume, compared to the density estimate at the $\sim 20,000 - 50,000$ locations of individual galaxies from DTFE as is a default in the DISPERSE workflow, given the same input (galaxy catalogs) in both density estimators. The density field produced by MPCM is, therefore, much higher resolution than that from DTFE, allowing for the characterization of density far from galaxies to voids. This makes the MPCM density field a natural candidate for the input density field in DISPERSE and, therefore, begs a comparison with the DTFE density field.

This has motivated us to apply the density field estimate of MPCM to the DISPERSE pipeline and to compare the output filamentary skeleton between the DTFE and the density field of MPCM. Specifically, in step 2 of the DISPERSE work-

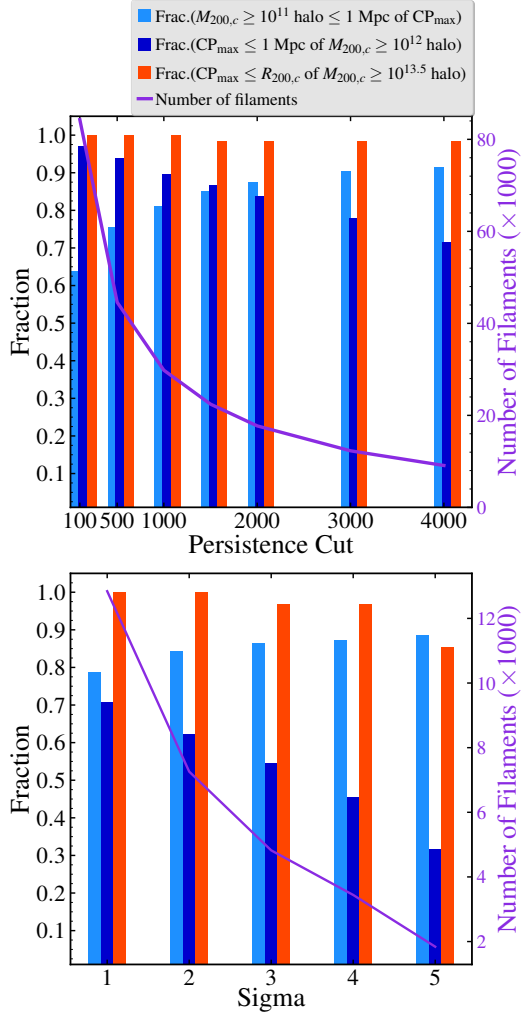


Figure 2. The results of experiments to determine the optimal persistence threshold (x-axis) in DISPERSE at $z = 0$, for the MPCM density field (top) and the DTFE density field (bottom). For the y-axis, the orange bars represent the fraction of $\log(M_{200,c}/M_{\odot}) \geq 13.5$ halos containing a node (CP_{\max}) within $R_{200,c}$, the dark blue bars show the fraction of CP_{\max} within 1 Mpc of a $\log(M_{200,c}/M_{\odot}) \geq 12$ halo, the light blue bars show the fraction of $\log(M_{200,c}/M_{\odot}) \geq 11$ halos within 1 Mpc of a CP_{\max} , and the purple curve denotes the total number of filaments identified for a given persistence cut. We choose persistence cut=1000 and sigma=2 as the fiducial persistence level of the reconstruction based on MPCM and the reconstruction based on DTFE, respectively (see text for details).

flow outlined in Section 2.2, we replace the density field estimate from DTFE with that of MPCM. To do this, we used our group’s custom-made PYSLIME software⁴ to read in the density field outputs for each TNG snapshot from MPCM. We then converted the binary files to regular 3D grids and smoothed them by downsampling by a factor of 2. This effectively reduced the spatial resolution of the density fields

⁴ <https://github.com/jnburchett/pyslme>

to approximately 0.5 Mpc, which smoothed the effect of the halo environment for all but the most massive halos. We experimented with increasing the grid downsampling factor to 4 and found that this had no effect on our reconstructed filaments or our statistical results. Next, we converted this smoothed grid to the native ND field format of DISPERSE using the *fieldconv* program. Finally, we use the *mse* program to identify critical points and the filamentary skeleton of the density field.

The identification of discrete structures in DISPERSE is mainly based on the persistence principle, meaning it must be robust to shot noise. Therefore, the persistence threshold is a critical factor in determining the confidence level of identified structures. However, assessing the accuracy and robustness of these structures presents a challenging problem, as any ideal reconstruction of the cosmic web must satisfy two criteria: (1) *completeness* to ensure identification of all filaments, and (2) *purity* to ensure that the identified filamentary structure is physically sound. To increase completeness, the persistence threshold can be reduced, resulting in the identification of more filaments. However, this may lead to the identification of spurious critical points and filaments not located near massive galaxies, which trace the peaks in the matter density field. The balance between completeness and purity of filamentary skeletons is discussed in detail, with numerous examples, in Sousbie (2011).

In a recent study of the MilleniumTNG simulation (Pakmor et al. 2023), Galárraga-Espinosa et al. (2023) presented a blueprint to calibrate the persistence threshold by physically motivated priors that address both the completeness and purity of the output skeleton. They found that optimal persistence maximized the fraction of massive groups/clusters that were near a maximum or node of the density field and the fraction of maxima that were near high-mass halos. We follow their approach and develop a physically motivated calibration of the optimal persistence threshold by varying the threshold and calculating several quantities for each threshold. These quantities include (1) the fraction of halos with $\log(M_{200,c}/M_{\odot}) \geq 13.5$ that contains a node (hereafter CP_{\max}) within their $R_{200,c}$, (2) the fraction of CP_{\max} within 1 Mpc of a halo with $\log(M_{200,c}/M_{\odot}) \geq 12$, (3) the fraction of halos with $\log(M_{200,c}/M_{\odot}) \geq 11$ within 1 Mpc of a CP_{\max} , and (4) the total number of filaments identified. For quantity (1), we opted to use a halo mass threshold of $\log(M_{200,c}/M_{\odot}) = 13.5$ instead of the higher $\log(M_{200,c}/M_{\odot}) \simeq 14$ threshold adopted by Galárraga-Espinosa et al. (2023) due to the very low number statistics of $\log(M_{200,c}/M_{\odot}) \geq 14$ mass halos in TNG100. For quantities (2) and (3), we choose a maximum separation of 1 Mpc between CP_{\max} and massive halos to account for the smoothing of the filamentary skeleton done in post-processing (see below).

To determine the optimal persistence threshold, we aim to maximize the quantities (1) through (4) mentioned above. We also analyze the distribution of comoving filament lengths, denoted by L_{fil} . This is done by calculating the length of each segment that makes up a filament for differ-

ent persistence thresholds. This helps us identify which reconstructions generate shorter or longer filaments. Following the instructions in the DISPERSE manual, we set the persistence level using the “-nsig” parameter, which indicates the number of sigmas used in *mse* for reconstructions based on the DTFE density field. This is the method used by the large majority of DISPERSE users. For reconstructions that use a non-DTFE (MCPM) density field, we use the “-cut” parameter, which is a numerical value of persistence.

The Figure 2 displays the results of our experiments conducted to determine the optimal persistence levels at $z = 0$. The bar charts represent fractions (1) through (3) for different persistence cuts for the MCPM density field (top) and different values of -nsig for the DTFE density field (bottom). The purple line indicates the total number of filaments identified for each run (values on the right vertical axis). The figure indicates that a higher persistence level leads to a higher fraction of $\log(M_{200,c}/M_{\odot}) \geq 11$ halos within 1 Mpc of a CP_{\max} , a lower fraction of CP_{\max} within 1 Mpc of a $\log(M_{200,c}/M_{\odot}) \geq 12$ halo, and a lower number of identified filaments. However, the fraction of large group/cluster-mass halos hosting a CP_{\max} within $R_{200,c}$ remains relatively constant.

Although it is difficult to define a precise numerical threshold for quantities that are considered to be “optimum” to maximize completeness and purity, it is important to ensure that we have a large percentage of approximate physical location matches between CP_{\max} and massive halos. For the MCPM density field runs, we tested cuts of 1000, 1500, and 2000 and found that all three cuts yielded matched fractions of $\gtrsim 80\%$. Although all three choices are suitable for an optimum persistence cut, we chose cut=1000 as our fiducial cut for three reasons. First, all halos with $\log(M_{200,c}/M_{\odot}) \geq 13.5$ contain CP_{\max} when we use cut=1000. Second, this cut identifies the most filaments out of the three cuts. Lastly, we found that cuts ≥ 1000 resulted in substantial populations of short filaments ($\lesssim 5$ Mpc), with cut=1000 giving the smallest median L_{fil} . More generous cuts gave much longer filaments on average, since the lower persistence connects filaments in even lower-density regions. We also performed visual verification and found no noticeable difference between the reconstructions for cut=1000, 1500, and 2000. Moreover, we found no qualitative change in our results when we changed the persistence cut. At redshifts $z > 0$, cut=1000 optimized our physical calibration criteria, which means that all massive groups/clusters host a CP_{\max} , massive halos are near CP_{\max} , and a large number of filaments are identified, including a substantial population of short filaments.

Our analysis shows that for the DTFE density field runs, a persistence cut of $\sigma = 2$ is optimal. This cut ensures that all halos with $\log(M_{200,c}/M_{\odot}) \geq 13.5$ contain a CP_{\max} , and more than 80% of halos with $\log(M_{200,c}/M_{\odot}) \geq 11$ are within 1 Mpc of a CP_{\max} . Additionally, this cut yields a substantial number of filaments (around 7000). Nevertheless, none of the sigma cuts produces a result where more than 80% of CP_{\max} is within 1 Mpc of a $\log(M_{200,c}/M_{\odot}) \geq 12$ halo, implying that a substantial fraction of CP_{\max} are not

near massive halos, a level we expect. This means that DTFE density field runs face significant challenges in associating massive halos to CP_{\max} . Our analysis also indicates that $\sigma = 2$ and $\sigma = 3$ produce similar results, and our choice of $\sigma = 2$ is the same as that of Galárraga-Espinosa et al. (2023) for their MilleniumTNG reconstruction. However, it differs from the cut $\sigma = 3$ that we used in Paper I based on previous work on TNG100. Finally, we emphasize the crucial observation that the MCPM density field runs identify an order of magnitude more filaments than the DTFE density field runs while maintaining accurate reconstruction of the skeleton through physical matching between CP_{\max} and massive halos. We will elaborate on this point in more detail below.

We also experimented with the smoothing parameter in the *skelconv* program. For our MCPM and DTFE density field runs, we applied a smoothing of 1, 2, and none to the filamentary skeleton (smoothing higher than 2 levels would wash out local geometrical structure of filaments). We found little to no impact on the visual structure of the reconstructed filaments and the qualitative results of the statistics of the filaments, such as the L_{fil} distribution. This finding is in contrast to what was stated in Galárraga-Espinosa et al. (2023). A similar conclusion was reached in Paper I. This smoothing technique averages the location of the individual points that make up a filament segment, as a filament segment is at most approximately 1 Mpc in length. Consequently, we consider this to be the maximum allowable separation between CP_{\max} and halo centers in the physical calibration experiments discussed previously. We have selected a smoothing of 1 as our fiducial value for both the DTFE and MCPM runs, as this reduces unphysically sharp filament segments, a fact that we verify visually.

2.5. DTFE vs. MCPM density field

After determining the best persistence and smoothing parameters for our two separate density field runs using DISPERSE, we compared the output of the filamentary structure in each. We began by visually comparing the differences between filaments identified from the regular DTFE density field and the new MCPM density field. In Figure 3, we present a 2D visualization of galaxies, the underlying DM density field, and the identified filaments from the input of the DTFE density field to *mse* (on the left) and the input of the MCPM density field (on the right). The same 10 Mpc thick slice is shown for the $z = 0$ snapshot of TNG. In both panels, the filaments are shown as curves colored by persistence value (more robust filaments are colored yellow), galaxies are represented by small gray circles, and the DM overdensity, $1 + \delta_{\rho}$ (DM), smoothed on a 1 Mpc scale and integrated along the 10 Mpc line of sight is colored white-to-blue (with darker regions indicating denser regions).

The change in the identified filamentary structure between the two density-field inputs is quite dramatic. The MCPM density field run can identify many more filaments, faithfully tracing the underlying DM distribution and connecting most galaxies. The DTFE density field run misses many less persistent filaments that its MCPM counterpart captures. The

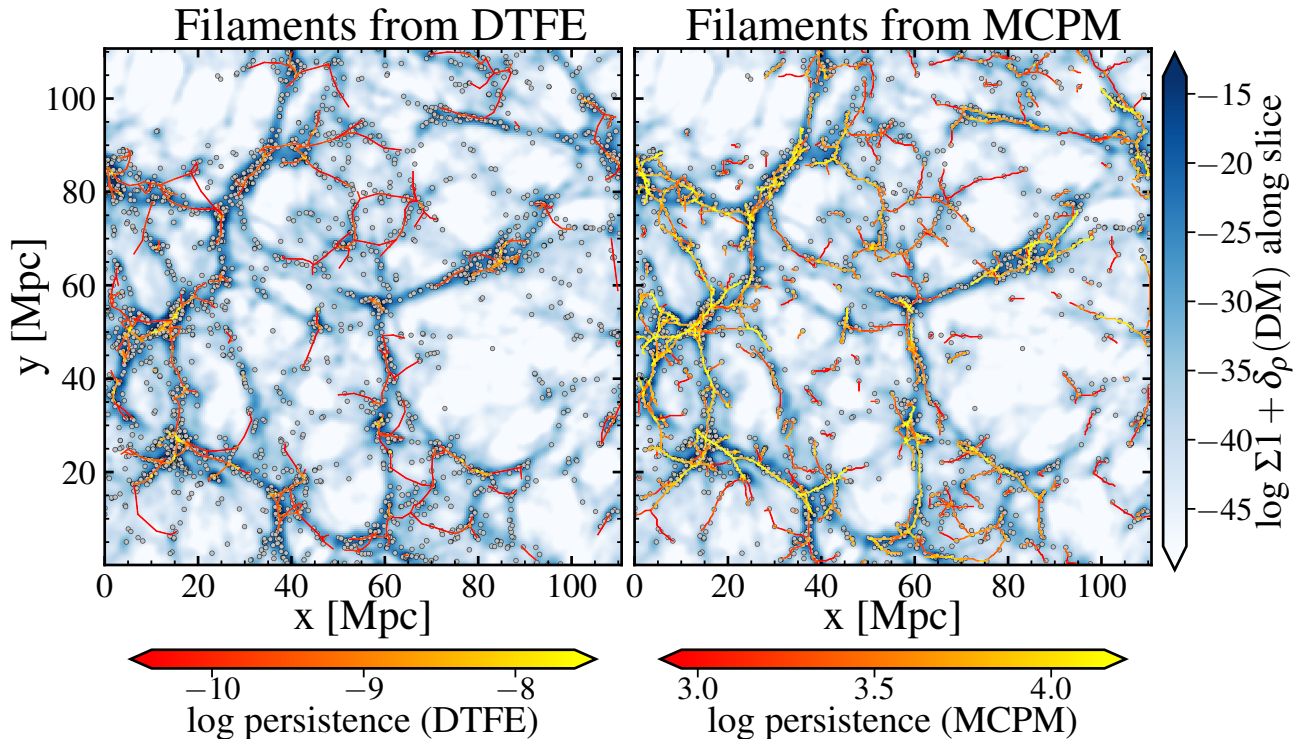


Figure 3. A 2D visual comparison of the filaments identified by DISPERSE from the DTFE density field (left) and the MCPM density field (right) in the same 10 Mpc thick slices in TNG100 at $z = 0$. In both panels, the underlying DM overdensity along the line of sight is represented by the blue-white colorbar, and gray circles represent galaxies. The filaments from DTFE and MCPM are color-coded curves by the persistence value (red is less persistent, yellow is more persistent). *The MCPM density field identifies the filamentary structure with significantly higher fidelity, including the less prominent filaments that the DTFE density field method misses.*

result is that DTFE only enables identifying the most persistent filaments (even for the relatively generous $\sigma = 2$ cut we adopt) and is only successful in connecting more massive galaxies. We also see that the shapes of the MCPM-based filaments appear to be much more natural, i.e., more curved shapes with very few sharp line segments, than those of the DTFE-based filaments. Several DTFE-based filaments appear very sharp or unphysical (e.g., looped filaments or filaments that do not follow the spatial distribution of the DM matter density). We find similar differences in the reconstructions at higher redshifts.

The accuracy of identifying the structure of the cosmic web has greatly improved by replacing the DTFE with the MCPM density field, both in terms of physically matching the matter density field as traced by $1 + \delta_\rho$ (DM) and finding less persistent filaments that should nevertheless connect galaxies based on visual inspection. This is due to MCPM’s strength in tracing the underlying matter density field across a wide dynamic range and identifying connections between galaxies within even diminutive structures. In other words, the MCPM density field provides a more complete description of the volume, while the DTFE density field only has values at the locations of input galaxies. Note, however, that both density field estimations were based on the same input galaxies. We conclude that injecting an MCPM density field into the main DISPERSE algorithm results in the identification of less prominent structures, as it provides a highly com-

plete density field estimate in addition to recovering the more prominent structures more reliably (see Figure 3 below).

Since we only have access to galaxy positions in the real universe, our method can be used to identify less prominent filaments in any observed galaxy survey. Reconstructing from DM/gas particles is impossible from an observational perspective and is not useful outside of the simulation domain. However, we know that using individual particles as tracers in simulations (as opposed to, e.g., galaxies) can increase the number of faint structures detected. Previous applications of the DTFE/DISPERSE method have demonstrated this fact (e.g., Kuchner et al. 2020; Kotecha et al. 2022). In Section 4.1, we briefly compare the output structure from using DM particles as tracers (in the DTFE algorithm) to that using galaxies as tracers (in the MCPM algorithm). Our method employs MCPM density fields and does not require a large number of particles as tracers. A relatively sparse catalog of galaxies is enough to identify the highly detailed filamentary structure that traces the underlying matter distribution with remarkable accuracy. This significantly reduces the storage and computational requirements for identifying less prominent filaments of the cosmic web (a $z = 0$ snapshot of TNG100 is 1.7 TB in size).

To show how well the MCPM-based filaments connect galaxies compared to DTFE-based filaments, we present a series of visualizations in Figure 4. The figure shows three different redshifts in three rows (top: $z = 0$, middle: $z = 1$,

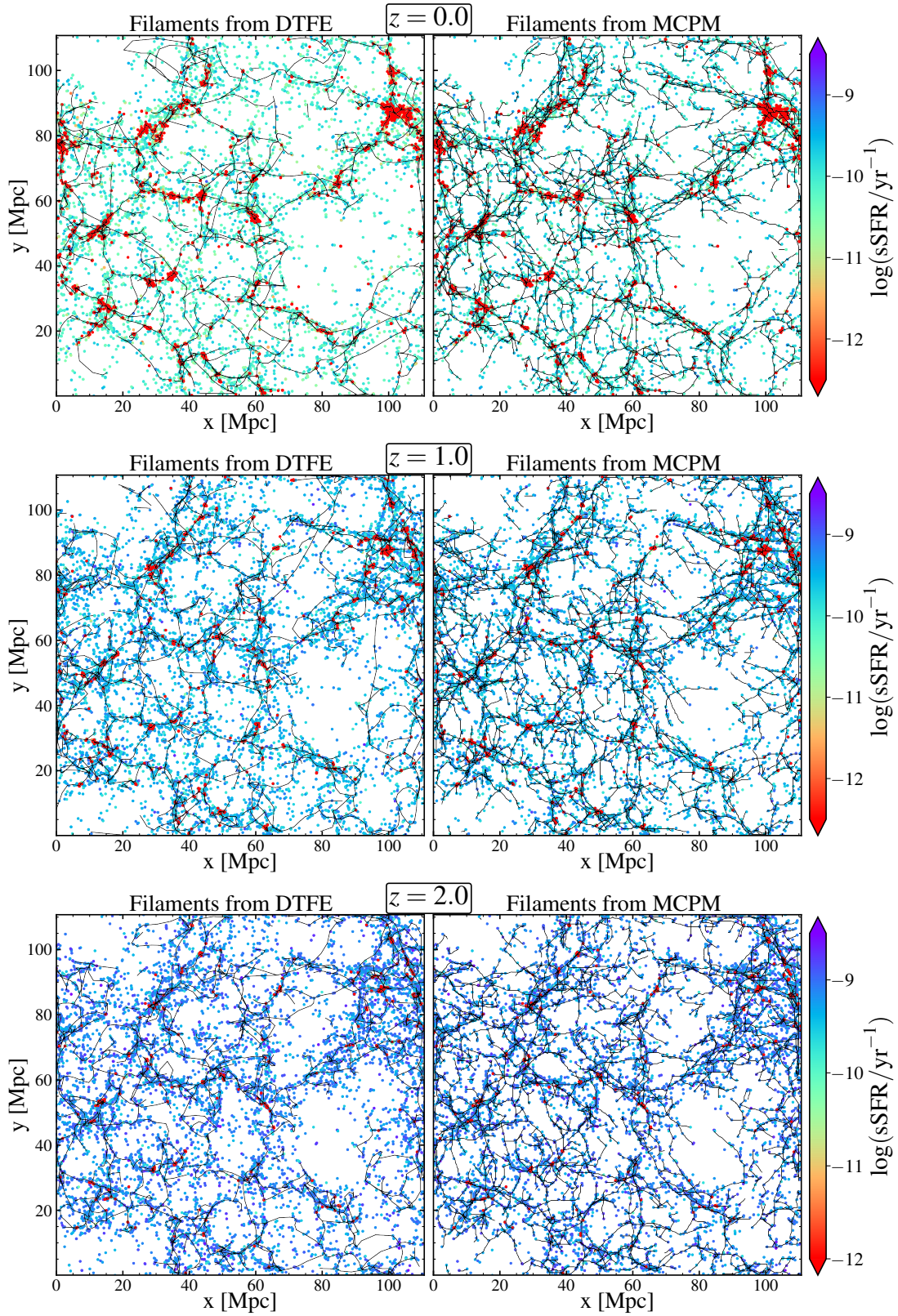


Figure 4. Visual comparison of the identified filamentary structure (black curves) from the DTFE (left) and MCPM (right) density fields overlaid on top of galaxies (dots), which are colored by sSFR at redshifts $z = 0$ (top row), $z = 1$ (middle row), and $z = 2$ (bottom row). MCPM-based filaments trace most of the galaxies, whereas DTFE-based filaments do not.

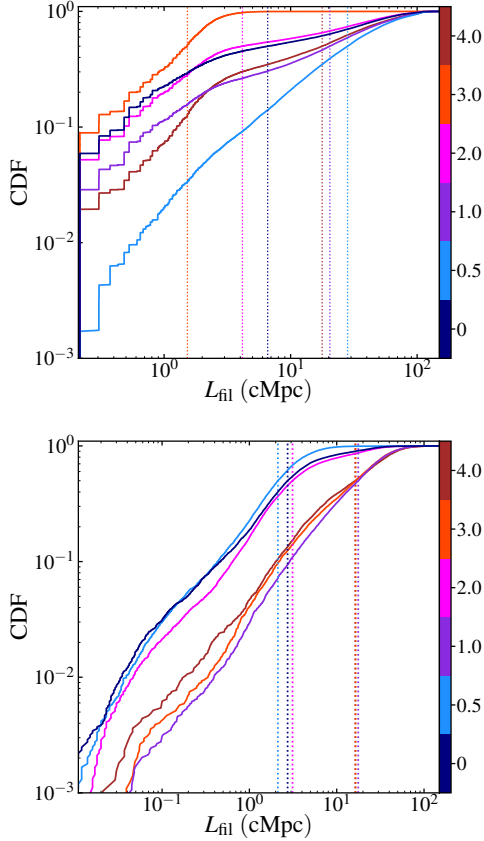


Figure 5. Cumulative distribution of total comoving length of filaments L_{fil} from MPCM (top) and DTFE (bottom) at different redshifts (each with a different color). The vertical dotted lines represent the median L_{fil} at a given z . Note that the two panels have differing scales on their horizontal axes.

bottom: $z = 2$). The filaments identified from the DTFE density field are presented in the left panels, while those identified from the MPCM density field are shown in the right panels, represented by thin black curves. Galaxies are colored by their specific star formation rate (sSFR) and sized by their stellar mass then. The same 25 Mpc thick slice is shown. The larger catalog of MPCM-based filaments connects most galaxies, whereas DTFE-based filaments leave many galaxies far from any identified structure. Moreover, MPCM-based filaments exhibit natural and physical shapes (curved and not sharp line segments) at these redshifts. DTFE-based filaments show some spurious features, notably a large, nearly vertical filament around $x \sim 92 - 95$ Mpc at $z = 1$, which does not appear to connect many galaxies. As we found in Paper I qualitatively, it appears that more quenched galaxies reside closer to filament spines for both cosmic-web reconstructions. This will be quantified in more detail below.

In Figure 5, we present cumulative distribution functions (CDFs) of the lengths of the comoving filaments L_{fil} from MPCM (top) and DTFE (bottom) at redshifts $z = 0, 0.5, 1, 2, 3$, and 4. Vertical dotted lines indicate the median L_{fil} values at given redshifts. On average, MPCM-based fila-

ments tend to be shorter, except at $z = 0.5$ when longer than DTFE-based filaments. The CDFs for MPCM-based filaments rise less sharply than those for DTFE-based filaments. MPCM-based filaments have a minimum L_{fil} of approximately 0.2 Mpc, while DTFE-based filaments have $L_{\text{fil}} < 0.1$ Mpc, which are unphysically small and likely spurious features instead of actual filaments. This is another advantage of filament identification with MPCM, as some DTFE filaments are simply artificial.

Finally, we compare the true underlying matter distribution and the output of the MPCM density field and DISPERSE. In Figure 6, we present the DM overdensity $1 + \delta_\rho$ (DM) as a function of the average persistence of MPCM filament segments (left) and the MPCM overdensity $1 + \delta_\rho$ (MPCM) at the midpoint of the segment (right) at $z = 0$. The dotted curves represent the middle 68% (16th–84th percentile) of the distribution. Average persistence is the average value of persistence at the two critical points of the extremities of the segment.

We find that persistence has a strong correlation with $1 + \delta_\rho$ (DM), with a Spearman correlation coefficient of 0.77. The relationship is almost linear (in logarithmic space), except for a steepening at high persistence. $1 + \delta_\rho$ (MPCM) also correlates quite well with $1 + \delta_\rho$ (DM), with a slightly lower Spearman correlation coefficient of 0.68. This confirms our earlier claim that the MPCM trace density maps quite cleanly onto the true matter density. At a fixed $1 + \delta_\rho$ (MPCM), the $\pm 1\sigma$ scatter is $\lesssim 0.5$ dex about the median relationship. The scatter increases at the highest $1 + \delta_\rho$ (MPCM), similar to persistence. The Spearman coefficient is slightly larger for the $1 + \delta_\rho$ (DM)– $1 + \delta_\rho$ (MPCM) relationship when the DM density field is smoothed on scales of 0.25 Mpc, which is comparable to the spatial resolution of the MPCM density field. The correlation worsens as the smoothing length increases. We chose 1 Mpc as it smooths out the effect of almost all halos. We stress again that the MPCM density estimate is not intended to be strictly a *physical* density, rather it is to be mapped to the true physical density as traced by DM. These results demonstrate that the distribution of cosmic matter is well traced by both the MPCM overdensity and the persistence of filaments from the MPCM density field in DISPERSE.

3. THE EFFECT OF FILAMENTS ON GALAXY EVOLUTION

3.1. How Filaments Affect Star Formation

Here, we study how the MPCM density field-based filaments of the cosmic web environment affect galactic star formation activity and gas fraction. The relationship is analyzed by selecting galaxies based on their stellar mass, redshift, and central/satellite status of galaxies.

3.1.1. sSFR vs. Filaments

First, we study the effect of filaments on the specific star formation rate (sSFR) of galaxies. To quantify the filamentary environment, we calculated the comoving transverse dis-

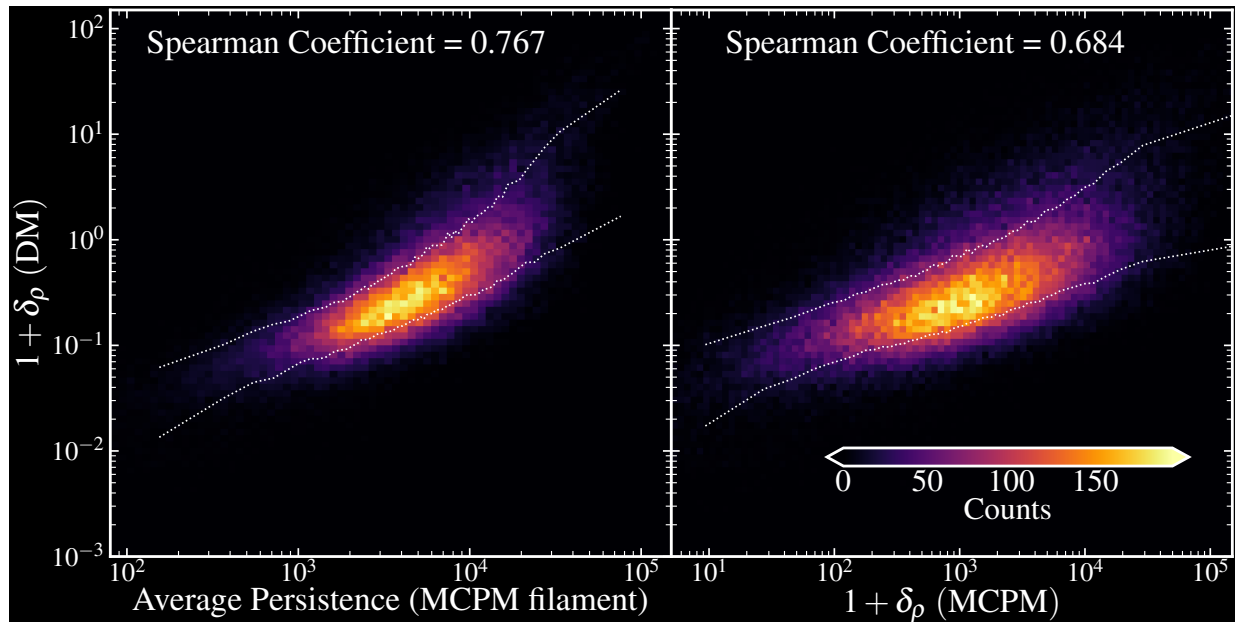


Figure 6. The $z = 0$ correlation between DM overdensity $1 + \delta_\rho$ (DM) and average persistence (left) and MCPM overdensity $1 + \delta_\rho$ (MCPM) (right) at the midpoint of filament segments. The dotted curves are meant to show the middle 68% of the distribution. The color bar on the right shows the mapping of color to number of points. Both persistence and $1 + \delta_\rho$ (MCPM) trace the underlying mass density well.

tance from each galaxy to the spine of the nearest identified filament, d_{fil} , similar to Paper I. We measured this distance for both the DTFE and MCPM methods, denoted as $d_{\text{fil}}(\text{DTFE})$ and $d_{\text{fil}}(\text{MCPM})$, respectively. For each of redshifts $z = 0, 0.5, 1, 2, 3$, and 4, we separate galaxies into three bins of stellar mass: $8 \leq \log(M_*/M_\odot) < 9$, $9 \leq \log(M_*/M_\odot) < 10$, and $\log(M_*/M_\odot) \geq 10$ and seven bins of $d_{\text{fil}}(\text{DTFE})$ and $d_{\text{fil}}(\text{MCPM})$. We then calculate the median sSFR, $\langle \text{sSFR} \rangle$, for each bin of $d_{\text{fil}}(\text{DTFE})$ and $d_{\text{fil}}(\text{MCPM})$ for a given mass range and redshift.

The results are presented in Figure 7. The top panels show $\langle \text{sSFR} \rangle$ as a function of $d_{\text{fil}}(\text{DTFE})$, and the bottom panels show $\langle \text{sSFR} \rangle$ as a function of $d_{\text{fil}}(\text{MCPM})$ for all galaxies. The left, middle, and right panels represent galaxies of stellar mass $8 \leq \log(M_*/M_\odot) < 9$, $9 \leq \log(M_*/M_\odot) < 10$, and $\log(M_*/M_\odot) \geq 10$, and the different sets of colored data points, error bars, and dotted curves represent $\langle \text{sSFR} \rangle$, $\pm 1\sigma$ bootstrapped errors on $\langle \text{sSFR} \rangle$, and spline interpolations of the $\langle \text{sSFR} \rangle$ - d_{fil} relation, respectively, at different redshifts. As in Paper I, some data points are presented as upper limits due to the minimum resolvable SFR = $10^{-2.5} M_\odot \text{ yr}^{-1}$ in TNG100 (Terrazas et al. 2020).

Our results show a striking difference between the MCPM and DTFE methods in terms of the dependence of the average star formation on d_{fil} . When DTFE-based filaments are considered, galaxies quench as they get closer to filaments at low redshift for all stellar masses. This is especially true at $z = 0$, where a decrease in $\gtrsim 2$ dex in sSFR occurs from high to low d_{fil} at any mass. In contrast, for MCPM-based filaments, there is virtually no dependence of $\langle \text{sSFR} \rangle$ on d_{fil} for all but $8 \leq \log(M_*/M_\odot) < 9$ galaxies at $z \leq 0.5$. Otherwise, when MCPM-based filaments are considered, *the distance to filaments appears to have almost no effect on star formation of*

high, intermediate, or low mass galaxies. This would conflict with the results in Paper I, which used the DTFE method for density fields. For both DTFE and MCPM filaments, there is no statistical correlation between median star formation and distance to filaments at $z \geq 2$.

The difference in our statistics between the two methods is perhaps unsurprising. We saw in Section 2.5 that qualitatively most galaxies are close to MCPM filaments, whereas many galaxies are not close to DTFE filaments. We quantitatively show this in Figure 8, which is a comparison of the CDFs for $d_{\text{fil}}(\text{DTFE})$ and $d_{\text{fil}}(\text{MCPM})$ at different redshifts. The vertical dashed line represents the median d_{fil} at a given redshift. On average, galaxies are significantly closer to a filament identified from MCPM than one identified from DTFE. The median $d_{\text{fil}}(\text{MCPM})$ is about 0.5 Mpc in all redshifts, while the median $d_{\text{fil}}(\text{DTFE})$ is $\sim 0.8 - 1.8$ Mpc. 90% of galaxies are within 1.5-2.5 Mpc (depending on redshift) of an MCPM filament, indicating that *virtually all galaxies live in or near a filament*. This is in line with the finding that the DTFE density field can identify only the most prominent filaments, while the MCPM method can identify filaments of much lower prominence. When filaments are identified with DTFE, a substantial fraction ($\approx 20 - 40\%$) of galaxies is found far from filaments ($d_{\text{fil}} > 3$ Mpc).

These findings motivate the need for a new metric by which to quantify the cosmic web environment that takes into account the effect of “thin” or low-density filaments and “thick” or high-density filaments. Unfortunately, the DISPERSE formalism does not allow characterization of filament widths, instead providing discrete point set outputs for locations of filament segments and critical points. We circumvent this problem by making use of the MCPM density. We define a new quantity, which we term the *filament line density*, or

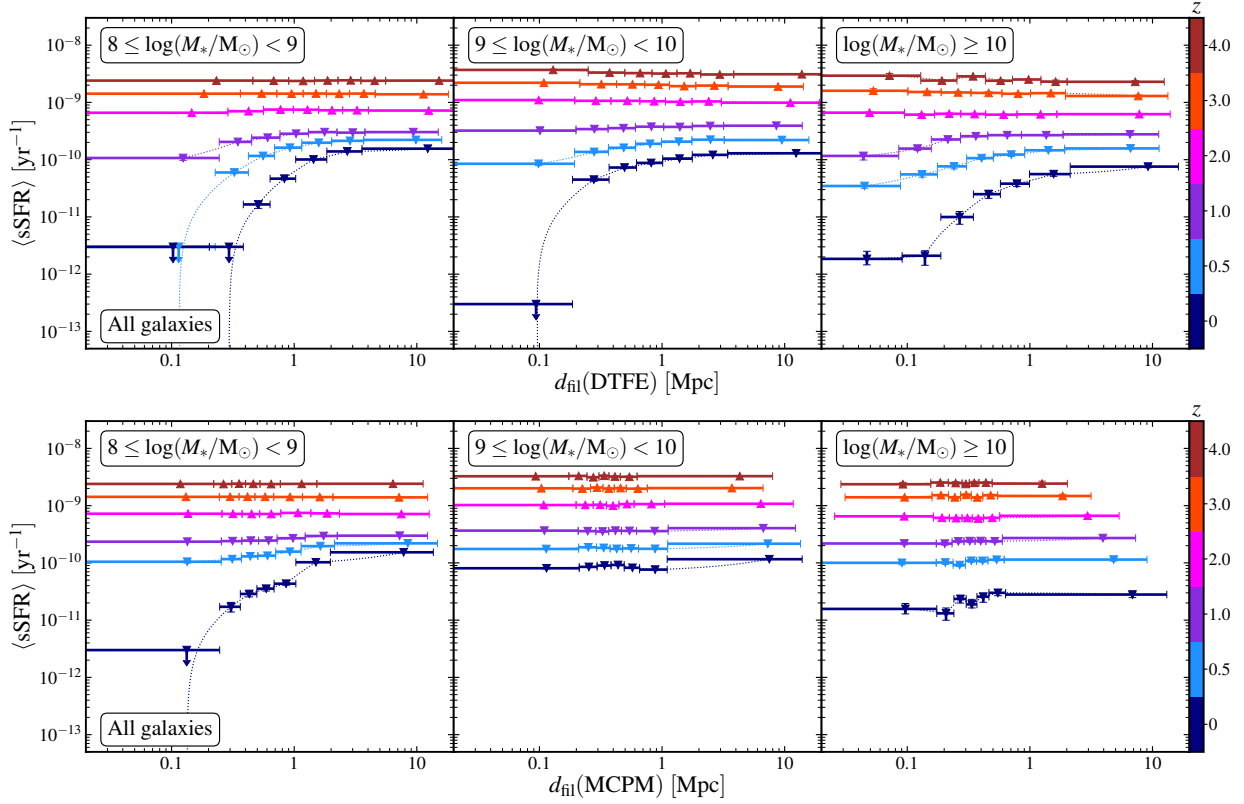


Figure 7. The median sSFR, $\langle \text{sSFR} \rangle$, as a function of distance to the closest filament identified from DTFE (top row) and MCPM (bottom row) for all galaxies of mass $8 \leq \log(M_*/M_\odot) < 9$ (left), $9 \leq \log(M_*/M_\odot) < 10$ (middle) and $\log(M_*/M_\odot) \geq 10$ (right) at redshifts $z = 0, 0.5, 1, 2, 3,$ and 4 as indicated by color bars on the left. We find very little correlation between $\langle \text{sSFR} \rangle$ and $d_{\text{fil}}(\text{MCPM})$ in almost all cases.

$\Sigma_{\text{fil}}(\text{MCPM})$,

$$\Sigma_{\text{fil}}(\text{MCPM}) = \frac{\sum_{\text{seg}} 1 + \delta_\rho(\text{MCPM})}{L_{\text{seg}}}, \quad (1)$$

where $\sum_{\text{seg}} 1 + \delta_\rho(\text{MCPM})$ is the sum of the MCPM overdensity in a filament segment, and L_{seg} is the physical length of the segment. $\Sigma_{\text{fil}}(\text{MCPM})$ is the summed overdensity per unit length of a filament segment and has dimensions of $1/\text{length}$. This quantity is a good descriptor of the *local* line density of filaments. It can depart significantly from the global line density as filaments can be ~ 100 Mpc long with significant variations in matter density along different segments. Although this quantity is not a direct measure of the physical filament density (which, again, would be impossible in the observational domain), we have already demonstrated that the overdensity of MCPM maps very well to the overdensity of matter of DM (Figure 6).

Past studies have used line density, filament width, or a similar metric to quantify filament thickness. Birnboim et al. (2016), in their analytical study of the hydrodynamic stability of filaments, analyzed the total filament mass per unit length. Zhu et al. (2022) used Hessian-based estimates of the cosmic web structure to identify wide and narrow filaments (which they term “prominent” and “tenuous”, respectively). Others, such as Ramsøy et al. (2021) and Galárraga-Espinosa et al. (2022), use simulation particle data to characterize typical density profiles and core widths of filaments. In contrast, the

approach we adopt here is designed to apply to observational data, for which both the MCPM density (and therefore $1 + \delta_\rho(\text{MCPM})$) and the lengths of the filament segment can be computed.

To test our hypothesis that filament line density is a measure of the thickness or prominence of a filament, we plot $\Sigma_{\text{fil}}(\text{MCPM})$ as a function of the average persistence of the critical points of a filament segment. This relationship is shown for six redshifts in Figure 9. The magenta line shows the median of the relationship at that redshift, and the dashed black line shows the median relation at $z = 0$. $\Sigma_{\text{fil}}(\text{MCPM})$ strongly correlates with persistence at each redshift (with Spearman correlation coefficients > 0.9 in all cases), and the median correlation changes only slightly with redshift. Line density increases monotonically with average persistence, indicating that the former is a good physical proxy to quantify the “prominence” of filamentary structures. With decreasing redshift, larger persistence values are seen, caused by high-persistence structures generated in increasingly high-density environments as groups and clusters take shape later in the universe.

For comparison, we also study the relationship between the persistence of the average filament and $\Sigma_{\text{fil}}(\text{DTFE})$, i.e., the filament line density of DTFE filaments. This relationship is shown for all six redshifts in Figure 10. We find that the increase in $\Sigma_{\text{fil}}(\text{DTFE})$ is not monotonic with persistence, unlike the increase in $\Sigma_{\text{fil}}(\text{MCPM})$. At low persis-

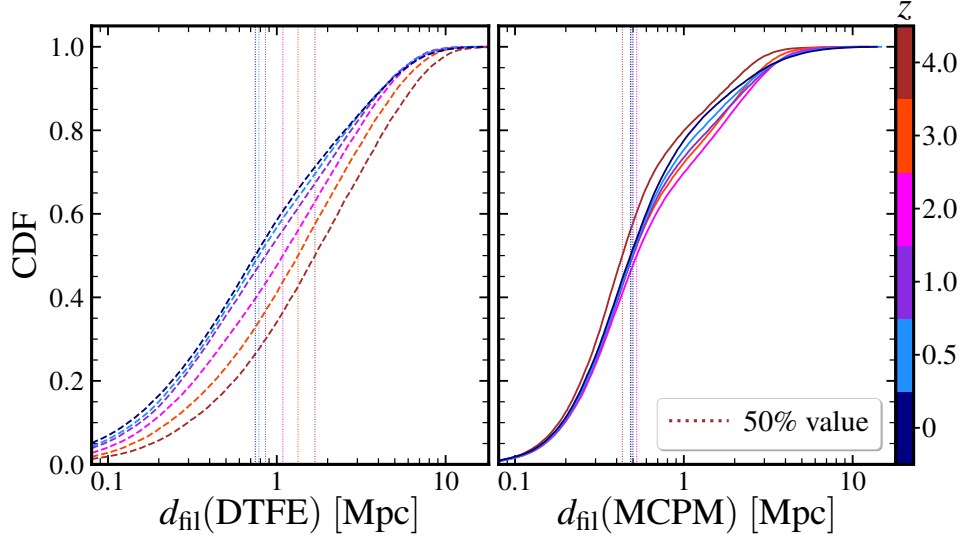


Figure 8. Cumulative distributions of $d_{\text{fil}}(\text{DTFE})$ and $d_{\text{fil}}(\text{MCPM})$ at different redshifts. For MCPM filaments, most galaxies live very close to a filament at any redshift, while many galaxies live very far from DTFE filaments.

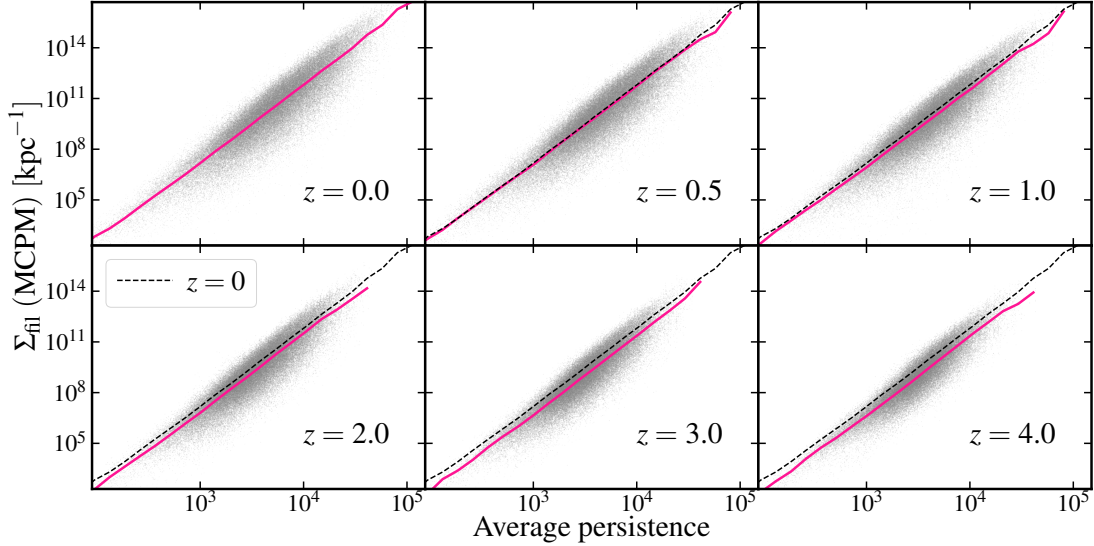


Figure 9. We see a strong monotonic correlation between $\Sigma_{\text{fil}}(\text{MCPM})$ and persistence at the midpoint of the filament segment at all z .

tence, there is a somewhat steep rise in $\Sigma_{\text{fil}}(\text{DTFE})$ with persistence, while at moderate and high persistence, there is a shallow rise with persistence. The scatter about the median $\Sigma_{\text{fil}}(\text{DTFE})$ -persistence relation is also larger than that of the median $\Sigma_{\text{fil}}(\text{MCPM})$ -persistence relation at any z or persistence. On further investigation, we find that the reason for this lack of monotonic correlation is that the DTFE filament segments are much longer than the MCPM filament segments. MCPM segments are always between ~ 0.2 and ~ 0.7 Mpc, while DTFE segments have a much larger range of $\sim 0.05 - 5$ Mpc, with most being ≥ 1 Mpc in length. Therefore, $\Sigma_{\text{fil}}(\text{DTFE})$ is less sensitive to local variation in filament density than $\Sigma_{\text{fil}}(\text{MCPM})$ and this results in a larger scatter. This is most likely a consequence of DISPERSE being able to identify less prominent filaments with MCPM, which can be shorter in low-density environments.

Indeed, we find that average persistence correlates well with the length of the segment for DTFE filaments.

Regardless, this analysis shows that more persistent filaments have a higher line density, but also that this depends on the identified filaments themselves. A less complete filament identification (such as that with DTFE) results in a line density parameter that does not capture the robustness of identified filaments and, therefore, is not a sufficient metric to quantify the filamentary environment. $\Sigma_{\text{fil}}(\text{MCPM})$, on the other hand, seems to be a good proxy for the width or thickness of the filament, as it captures the robustness with which a filament is identified and gives a good estimate of the local filament overdensity per unit length. $\Sigma_{\text{fil}}(\text{DTFE})$ is further flawed as a measure of a galaxy's cosmic web environment, as we have already shown that a large fraction of galaxies live far from a DTFE filament such that the nearest

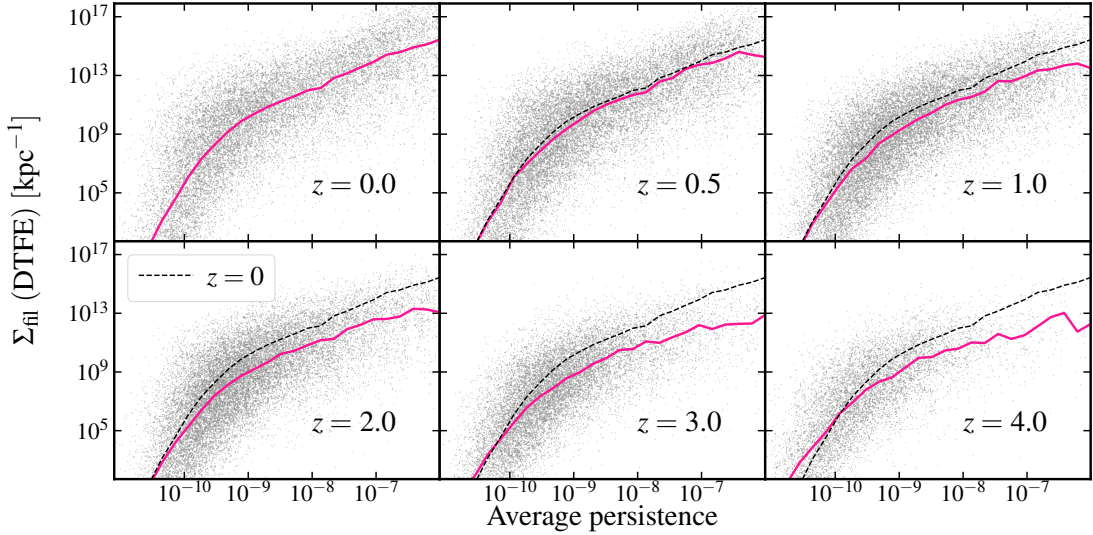


Figure 10. Same as Figure 9 but for Σ_{fil} (DTFE). DTFE filaments do not monotonically increase in line density with average filament persistence, unlike MCPM filaments.

such filament to a galaxy may not be physically associated with that galaxy.

We repeat our calculations of $\langle \text{sSFR} \rangle$ at different masses and redshifts as functions of Σ_{fil} (MCPM). In Figure 11, we present $\langle \text{sSFR} \rangle$ for different masses and redshifts as functions of Σ_{fil} (MCPM) of the closest filament segment for all galaxies (top panels), central galaxies only (middle panels) and satellite galaxies only (bottom panels). As in Figure 7, data points and error bars represent $\langle \text{sSFR} \rangle$ and their bootstrapped errors $\pm 1\sigma$, and some points are shown as upper limits. To be consistent with our previous plot, the line density increases to the left-hand side of each panel, i.e., the filaments become thicker to the left and thinner to the right.

We find that galaxies are generally quenched when they live near high-line density or thicker filaments at later times. Low-mass galaxies are the most strongly affected: even at $z = 1$, there is almost an order of magnitude suppression of star formation as these galaxies live near thick filaments (Σ_{fil} (MCPM) $\gtrsim 10^9 \text{ kpc}^{-1}$). At $z = 0$, galaxies of all masses are quenched if they live in or around such thick filaments. The effect of living near thick filaments starts to decrease with redshift; however, a slight decline of $\langle \text{sSFR} \rangle$ at the highest line densities is seen out to $z = 4$ for high-mass galaxies.

For lower-mass ($\log(M_*/M_\odot) < 10$) galaxies, satellites almost exclusively drive the Σ_{fil} (MCPM)-dependence of star formation activity. Low- and intermediate-mass satellites in thick filaments stop forming stars at $z \leq 1$, while centrals of the same mass feel virtually no effect of Σ_{fil} (MCPM), albeit only a mild reduction in $\langle \text{sSFR} \rangle$ for $8 \leq \log(M_*/M_\odot) < 9$ centrals in thick filaments at $z = 0$. For lower-mass satellites, the dependence is seen to be $z = 2$. For high-mass galaxies, on the other hand, both centrals and satellites feel the effect of filament thickness. $\log(M_*/M_\odot) \geq 10$ satellites experience a > 1 dex drop in $\langle \text{sSFR} \rangle$ in thicker filaments at $z \leq 0.5$, and $\log(M_*/M_\odot) \geq 10$ centrals see such a drop in $\langle \text{sSFR} \rangle$ at $z = 0$ (with the effect at $z = 0.5$ being less strong

but still quite significant). For the central and satellites in this mass range, a non-negligible dependence of $\langle \text{sSFR} \rangle$ on Σ_{fil} (MCPM) persists to $z = 4$. However, we note that the lower number of $\log(M_*/M_\odot) \geq 10$ satellites at $z \geq 3$ is a significant source of uncertainty.

The dashed curves in each of the plots above represent the best-fit relationship between $\langle \text{sSFR} \rangle$ and Σ_{fil} (MCPM) for the following functional form,

$$Y(X) = Y_0 \left(1 + \left(\frac{X}{X_0} \right)^\alpha \right)^\beta, \quad (2)$$

where $Y = \langle \text{sSFR} \rangle$, $X = \Sigma_{\text{fil}}$ (MCPM), X_0 is the Σ_{fil} (MCPM) value where the $\langle \text{sSFR} \rangle$ starts to decline from its characteristic value Y_0 , and α and β are power-law exponents. This is equivalent to the generic β model that has historically been used to model the gas density profile of galaxy clusters (e.g., Cavaliere & Fusco-Femiano 1978), but has also been applied in the context of gas density and galaxy profiles in filaments (e.g., Bonjean et al. 2020; Galárraga-Espinosa et al. 2022). In Eq. 2, we substitute the typically used radius in these models for the density of the filament line. While we have adopted this functional form, we note that some other models, such as the generalized NFW (e.g., Nagai et al. 2007) and the Einasto model (e.g., Einasto 1965), may also describe the relationships that we see quite well.

In any case, the functional form we choose is a good description of our qualitative trends: $\langle \text{sSFR} \rangle$ stays roughly constant until a truncation point in Σ_{fil} (MCPM), above which it drops as a power law described by some exponent. The best-fit parameters Y_0 , X_0 , α , and β change with redshift, stellar mass, and central/satellite status. At higher redshifts, the average star formation is higher, so Y_0 is higher, and the density threshold where $\langle \text{sSFR} \rangle$ drops is higher, so X_0 is also higher. Furthermore, the relationship flattens with increasing redshift, thus decreasing the magnitude of the slope β . We find that $\alpha \simeq 1$ in most cases, for which Eq. 1 can be approximated as a three-parameter model.

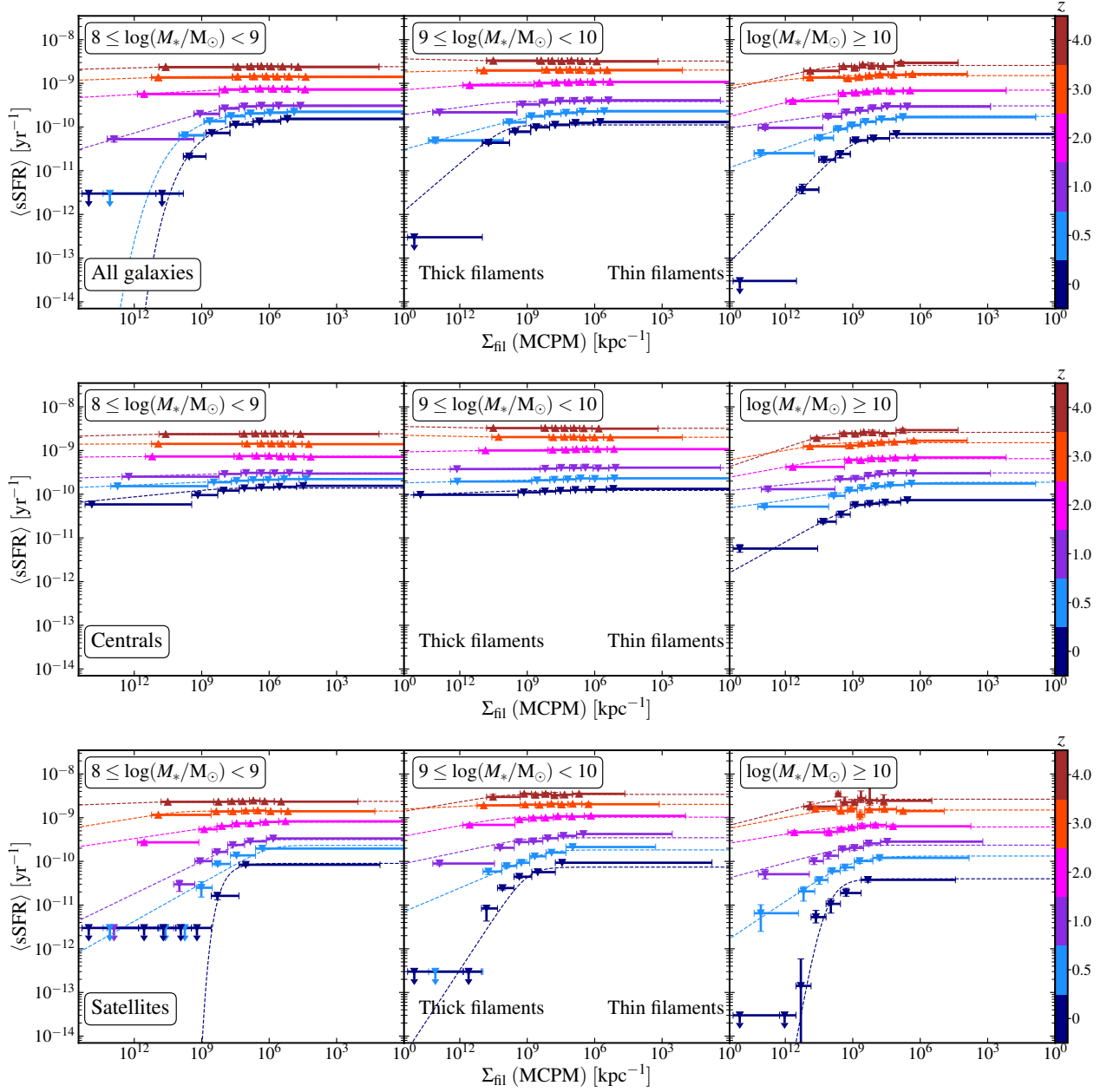


Figure 11. $\langle \text{sSFR} \rangle$ as a function of the filament line density Σ_{fil} (MCPM) (Eq. 1) for all galaxies (top row), central galaxies (middle row) and satellite galaxies (bottom row). The mass ranges, and redshifts are the same as in Figure 7. *Thick filaments quench galaxies at lower redshifts, thin filaments do not quench galaxies at all.*

Although we showed that virtually all galaxies live very close to MCPM filaments, we also applied $d_{\text{fil}}(\text{MCPM})$ cuts on the $\langle \text{sSFR} \rangle$ - Σ_{fil} (MCPM) relationships above. Choosing only galaxies within 1 or 2 Mpc of MCPM filaments, we recomputed $\langle \text{sSFR} \rangle$ as a function of Σ_{fil} (MCPM). As expected, we do not observe qualitative changes in the $\langle \text{sSFR} \rangle$ - Σ_{fil} (MCPM) relationship for any z or M_* .

3.1.2. Quenched/Red Fraction vs. Filaments

Median star formation is one indicator of the star formation activity of a population, but many others are used in the literature. Here, we assess the cosmic web dependence of the

red fraction, the fraction of galaxies with photometric colors below a certain threshold – and the quenched fraction, the fraction of galaxies with sSFR below a certain threshold. Similar to the observational studies of Peng et al. (2010) and Peng et al. (2012), we study the joint dependence of red and quenched fractions of galaxies on mass and environment to understand the relative importance of internal vs. external properties of galaxies in quenching them. Unlike these studies, however, we quantify the environment using filament line density as defined in the previous section. We calculate the red fraction as the fraction of galaxies with $g - r > 0.6$ (where g and r are SDSS photometric filters; Stoughton et al.

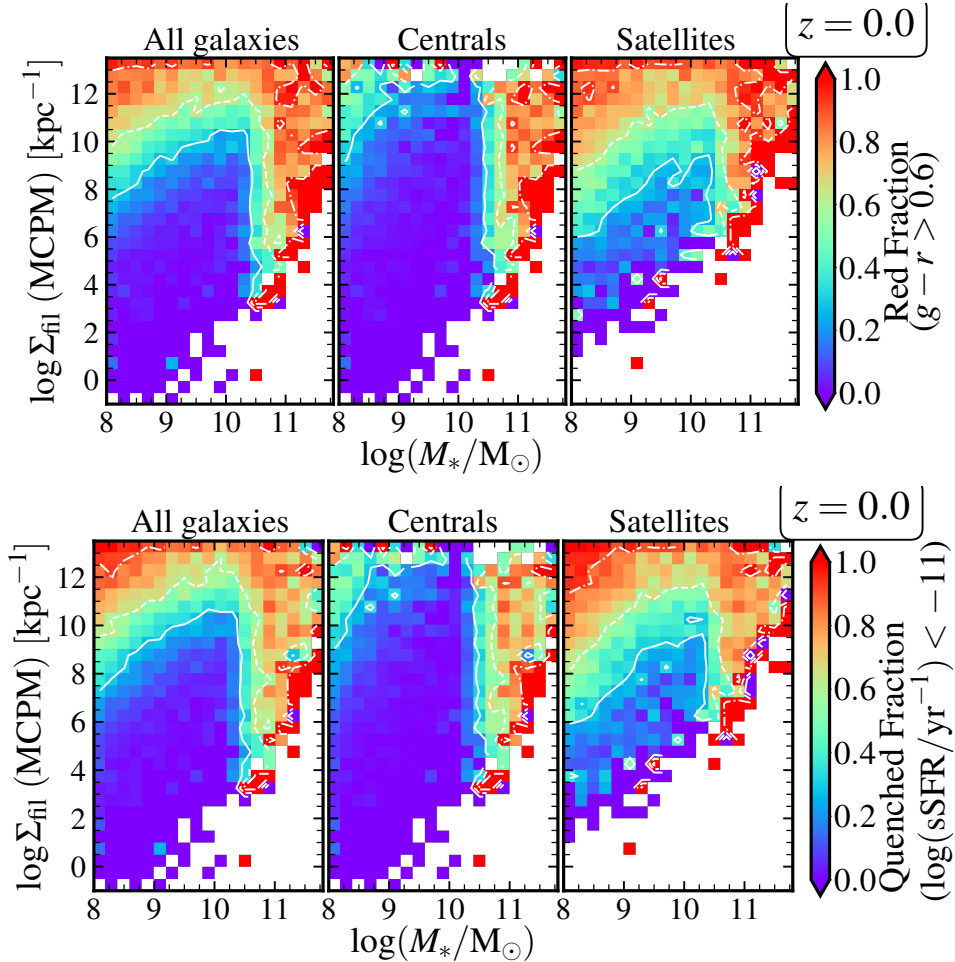


Figure 12. The median red fraction (top; fraction of galaxies with simulated colors $g - r > 0.6$) and median quenched fraction (bottom; fraction of galaxies with $\log(\text{sSFR}/\text{yr}^{-1}) < -11$) at $z = 0$ for all galaxies (left), centrals (middle), and satellites (right) as a function of stellar mass and filament line density. At high masses, most galaxies are quenched regardless of the filamentary environment. Lower-mass galaxies quench at lower line density than higher-mass galaxies. Satellites are strongly affected by the environment, whereas centrals are hardly affected.

(2002)). We adopted this color cut based on (1) the separation of red sequence and blue cloud galaxies in the well-known galaxy color bimodality observed at low redshift (e.g., Kauffmann et al. 2004), and (2) the excellent agreement between observed and simulated $g - r$ colors at $z < 0.1$, as well as the separation of red and blue galaxies for TNG100 at $g - r > 0.6$ reported by Nelson et al. (2018). We also calculate the quenched fraction as the fraction of galaxies with $\log(\text{sSFR}/\text{yr}^{-1}) < -11$, based on the commonly used criterion to separate star-forming and quenched galaxies in the local universe (e.g., Bluck et al. 2020; Donnari et al. 2021).

We bin galaxies in stellar mass and filament line density and measure the median red and quenched fractions as defined above in each 2D M_* - Σ_{fil} (MCPM) bin. The median red fraction (top panels) and quenched fraction (bottom panels) are presented for $z = 0$ in Figure 12. The left, middle, and right panels show all galaxies, centrals, and satellites, respectively. 30%, 60%, and 90% are shown as solid, dashed, and dashed-dotted curves, respectively, in each panel.

Considering the red fraction, we first note that most galax-

ies are red at $\log(M_*/M_\odot) > 10.5$, regardless of the filamentary environment. This is in agreement with Peng et al. (2010), despite slightly different definitions of the red fraction and environmental density (they used a galaxy number density). This is primarily a consequence of the AGN feedback model in TNG, which is known to quench galaxies very rapidly as their central BHs reach a mass of $\sim 10^{8.2} M_\odot$ (e.g., Terrazas et al. 2020; Zinger et al. 2020). In the highest-line density filaments ($\Sigma_{\text{fil}} \text{ (MCPM)} \gtrsim 100 \text{ kpc}^{-1}$), the vast majority of galaxies are red, albeit lower-mass centrals are bluer even in these environments. In line with the findings of Peng et al. (2012), satellites are the most susceptible to the environment (but once again, our findings are in terms of *filamentary* environment). At $\log(M_*/M_\odot) < 10.5$, for a fixed-line density, satellites are much redder on average than centrals. The qualitative results here do not change if we adopt slightly different cuts for the red fraction, e.g., $g - r > 0.55$ or $g - r > 0.65$. However, increasing the definition color threshold to higher values leads to a graph that qualitatively shows similar red fractions as quenched fractions for given

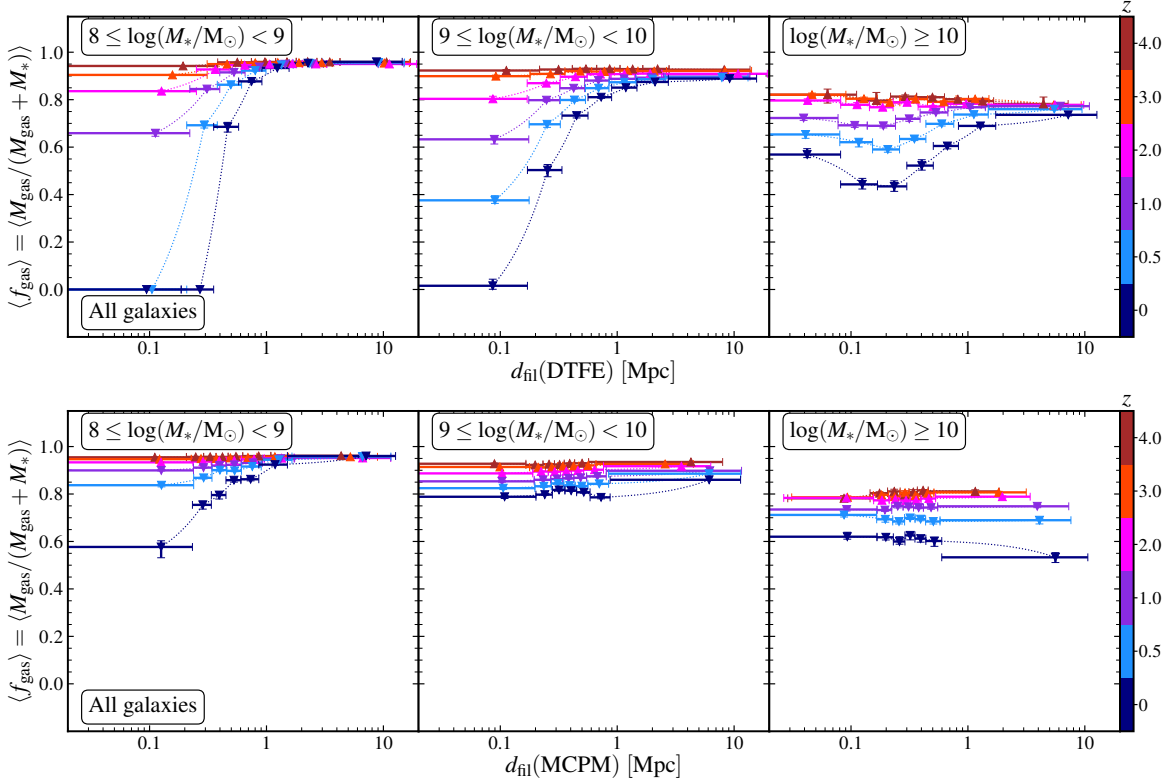


Figure 13. Same as Figure 7, but for the median f_{gas} , $\langle f_{\text{gas}} \rangle$. Distance to the MCPM filaments does not have a big effect on f_{gas} .

M_* and Σ_{fil} (MCPM).

Considering the quenched fraction, mass is once again the dominant factor at $\log(M_*/M_\odot) > 10.5$. Most galaxies are quenched above this mass, regardless of their nearby filament. On the contrary, at $\log(M_*/M_\odot) < 10.5$, most centrals are star-forming, regardless of Σ_{fil} (MCPM). The transition of galaxies from more star-forming to more quenched (bluer to greener colors) at fixed M_* occurs at higher Σ_{fil} (MCPM) with increasing M_* , from $\log(M_*/M_\odot) = 8$ to $\log(M_*/M_\odot) \sim 10.5$, implying that lower mass galaxies can quench in thinner filaments than higher mass galaxies. This is driven by satellites, which transition from star formation to quenched at very low Σ_{fil} (MCPM). We verified that changing the definition of the quenching threshold, e.g., to 0.5 or 1 dex below the star-forming main sequence, does not qualitatively impact our results. The near-identical results for the quenched and red fractions show that these are nearly equivalent measures of quenching, and offers a simple test to compare against observations.

Aside from constraining the relative effect of mass and filament line density in quenching galaxies in the local universe, the results in this section also demonstrate how the filament line density Σ_{fil} (MCPM) is an effective metric to quantify the environmental dependence of quenching. It is a viable alternative to local environmental measures characterized by the distance to N^{th} nearest neighbor or galaxy number density used by Peng et al. (2010), Peng et al. (2012), Darvish et al. (2014), and many others. When we repeated this analysis in terms of MCPM overdensity, itself a measure of local environment, we find that it does not so clearly sepa-

rate quenched/red galaxies from star-forming/blue galaxies as Σ_{fil} (MCPM) does. We shed further light in this section on the relative contribution of galaxy mass (an internal property) and filament line density (an environmental/external property) at $z = 0$ in TNG.

3.2. Gas Fraction vs. Filaments

The effect of filaments on quenching star formation in galaxies is complex, with many potential physical mechanisms at play. Here, we consider one of the more straightforward explanations: the availability of gas varies with the cosmic web environment. To this end, we measure the bound gas fraction of a galaxy, $f_{\text{gas}} = M_{\text{gas}} / (M_{\text{gas}} + M_*)$, similar to Hasan et al. (2023), and study its dependencies on the distance and density of the nearest filaments of the cosmic web. f_{gas} contains all gas particles gravitationally bound to a halo and can be considered the gas fraction of the circumgalactic medium (CGM).

We first present in Figure 13 the median gas fraction, $\langle f_{\text{gas}} \rangle$, as a function of d_{fil} for DTFE filaments (top) and MCPM filaments (bottom) in the same mass and redshift ranges as in section 3.1.1. The difference in the median $f_{\text{gas}}-d_{\text{fil}}$ relationship between the two methods is staggering. For DTFE filaments, the gas fraction drops by a factor of few from $d_{\text{fil}} \sim 1$ Mpc to $d_{\text{fil}} \sim 0.1$ Mpc at $z \leq 0.5$ for lower-mass galaxies. For high-mass galaxies, there is a smaller decline at those redshifts, followed by a difficult-to-explain rise at very low d_{fil} . This was shown to be an effect of the nearby nodes (CP_{max}) in Paper I. In contrast, for MCPM filaments, there is little dependence of $\langle f_{\text{gas}} \rangle$

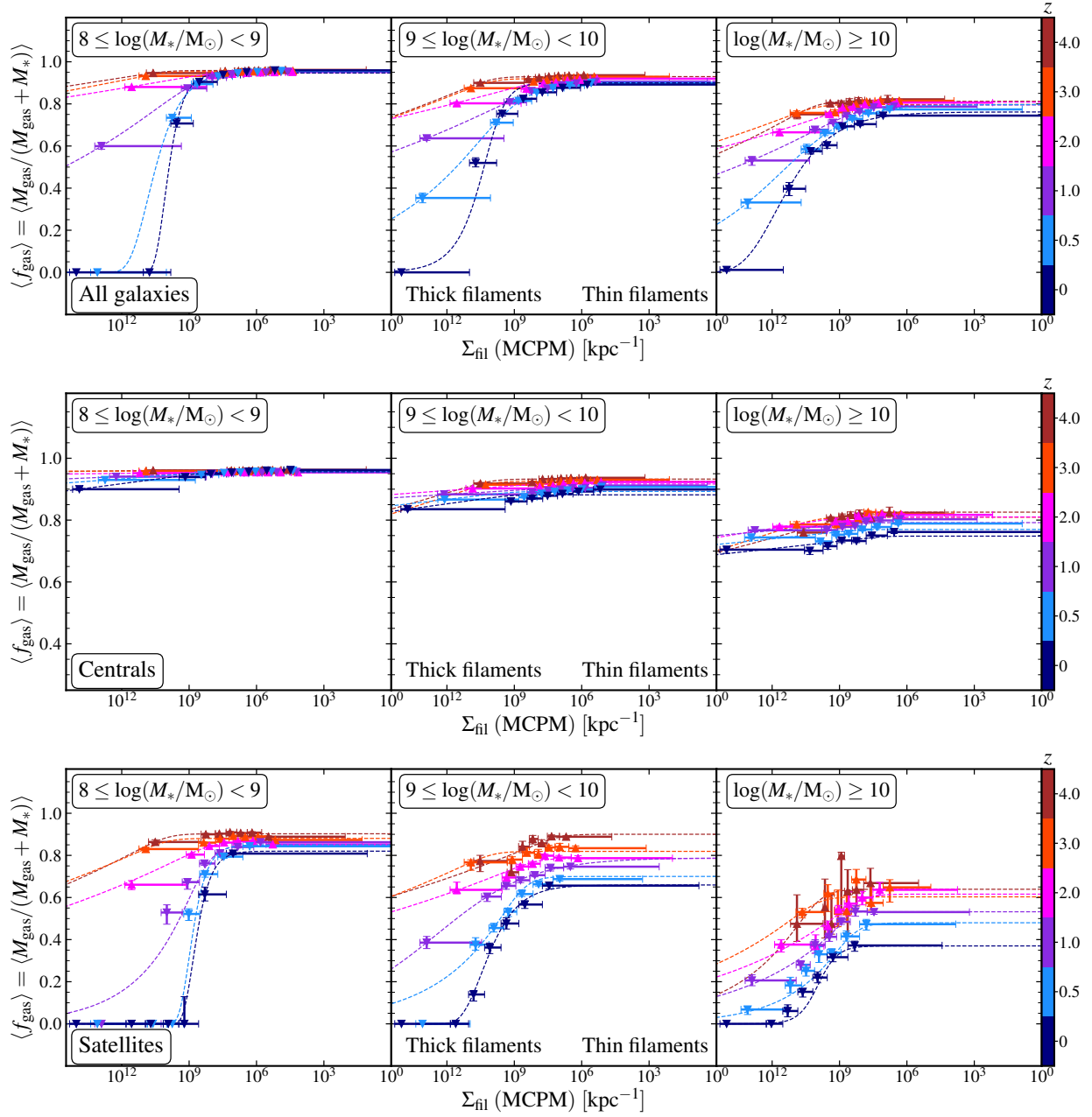


Figure 14. Same as Figure 11, but for $\langle f_{\text{gas}} \rangle$. The gas fraction correlates strongly with the filament line density at lower redshifts, but the correlation is mostly driven by satellites.

on d_{fil} , with just $8 \leq \log(M_*/M_\odot) < 9$ galaxies at $z = 0$ showing a considerable decline with proximity to filaments. There is even a small rise in $\langle f_{\text{gas}} \rangle$ with decreasing d_{fil} for $\log(M_*/M_\odot) \geq 10$ galaxies at $z = 0$. Interestingly, no such rise was observed in the $\langle \text{sSFR} \rangle$ of high-mass galaxies in Figure 7, for d_{fil} (DTFE) or d_{fil} (MCPM). Tentatively, this implies that high-mass galaxies have lower star-formation efficiency near the cores of filaments at lower redshifts.

Next, we perform the same measurements of $\langle f_{\text{gas}} \rangle$ in terms of Σ_{fil} (MCPM) and present the results in Figure 14. As in Figure 11, we present the relationship $\langle f_{\text{gas}} \rangle$ - Σ_{fil} (MCPM) for all galaxies (top), central galaxies (middle)

and satellite galaxies (bottom) for three different mass ranges and six different redshifts. The data points and error bars represent the medians and bootstrapped errors, respectively, and the dashed curves represent the best-fit relationships of the functional form in Eq. 2, where now $Y = \langle f_{\text{gas}} \rangle$ and Y_0 is the value of $\langle f_{\text{gas}} \rangle$ at X_0 . There is a pronounced decline in the median gas fraction with increasing filament line density for all masses at redshifts $z \leq 1$. At $z = 0$, there is very little gas on average in galaxies living in the thickest filaments, which explains the corresponding lack of star formation in these regions. However, this is caused by satellite galaxies, whose gas fractions strongly depend on Σ_{fil} (MCPM)

for all masses. On the other hand, the gas fractions of centrals are almost independent of Σ_{fil} (MCPM) across mass and redshift. Interestingly, we saw a noticeable decline with Σ_{fil} (MCPM) in $\langle \text{sSFR} \rangle$ of centrals of high mass at $z \leq 0.5$ in Figure 11 (middle row). Thus, massive centrals at later times likely have physical mechanisms acting on their gas supplies in the thickest filaments that reduce their star formation efficiency. Finally, we note that the median gas fraction has a non-negligible dependence on line density up to $z = 4$ for all galaxies, satellites, and high-mass centrals. The same is not true for the median sSFR, implying differential star formation efficiencies in different cosmic web environments. For satellites, most of the filament line density dependence of star formation can be explained by the corresponding dependence on the gas content of galaxies. We further discuss the difference in star formation efficiencies in different filamentary environments below.

4. DISCUSSION

4.1. Improved Cosmic Web Reconstruction

We showed that the identification of cosmic web structures is greatly improved when using the MCPM density field in DISPERSE instead of the prepackaged DTFE density field. In particular, filaments are identified with much higher fidelity than the MCPM density estimate. Firstly, much lower persistence structures are identified, revealing an entire population of low-line density, thin filaments that the DTFE-based method entirely misses (see further discussion in the next section). The same regions of space that would be considered voids from the DTFE method are shown to contain a small number of thin, diffuse filaments with the MCPM method. Second, the MCPM filaments perform significantly better connecting galaxies than the DTFE filaments. Third, the morphology of MCPM filaments is much more natural and physically robust (with rounded curves instead of line segments) than that of the DTFE filaments, which clearly show some unphysical shapes. Finally, from DTFE, we get a non-negligible fraction of very short filaments ($L_{\text{fil}} < 0.1$ Mpc), while MCPM, yields no such unreasonably short filaments.

There are several potential reasons why the MCPM density field drastically improves upon filament identification. The primary reason is the difference in sparsity of the DTFE and MCPM density fields, where the latter is a continuous estimate at all locations of the input volume (i.e., every $(0.5 \text{ Mpc})^3$) and the former only provides density estimates at the locations of galaxies (i.e., $\approx 1/10000$ of the information contained in the MCPM density field). Effectively, this means that the *mse* structure extractor in DISPERSE has a much more complete density field from which to compute gradients, local minima, maxima, and saddle points, which allows the topological identification scheme to recover underlying structures much more faithfully.

We comment that DTFE could produce density estimates at the same locations as MCPM. However, these would be local linear (or for some variants, quasi-local for a given kernel) estimates. DTFE is a local linear (or, low order polynomial) smoother; and invertible (apart from degenerate triangula-

tions). DTFE is robust and unbiased, but that means it can be significantly underutilizing its input information (if there is supplementary physical information it is ignoring). While MCPM is only probabilistically invertible, it can be hugely advantaged by its nonlinear representational capacity and its ability to be physically calibrated. This is the source of its expected information theoretic advantage; it is a biologically inspired machine learning model (which can tap the considerable amount of information in the latent space of galaxy catalogs). An additional comment is that a standard DTFE density field estimation is not weighted by mass, whereas that of MCPM is. Thus, MCPM is considerably advantaged over DTFE due to its expressivity, physically-motivated calibration, and sensitivity to masses. We defer a detailed comparison of a mass-weighted DTFE density estimation with the MCPM estimation from point datasets to future work.

Zakharova et al. (2023) found that the choice of tracers has a significant effect on the number of filaments identified by DISPERSE. Input galaxies are biased tracers of the cosmic mass distribution and do not identify some of the filaments that reconstructions based on DM particle input find. They also showed that filaments identified from DM tracers are, on average, longer than those identified from galaxy tracers. In our work, the input tracers are the same between the two methodologies (albeit with different intermediate density estimations). Still, similar differences are seen between identified filaments between the DTFE and MCPM density fields. Therefore, increasing the information in the density field improves the identification of filaments. We reran the DISPERSE filament identification using DTFE density estimation from DM particles as tracers instead of galaxies. The resulting outputs, depending on the adopted persistence threshold, show filamentary structures similar to those of our MCPM density field run on galaxies as tracers. We verified that both the visual and statistical comparisons between the output structures generated from DM particle tracers using DTFE and galaxy tracers using MCPM produce very similar qualitative results. In other words, the conclusions of our paper do not change between density estimation with DTFE using DM particles and that with MCPM using galaxies.

In the real universe, we do not have access to a continuous DM mass distribution, which traces the *true* cosmic matter distribution. Instead, we can only access sparser tracers, such as spectroscopically surveyed galaxies. We have shown that the MCPM overdensity maps very well to the DM overdensity across a broad range of cosmic density regimes, therefore serving as an excellent proxy for the cosmic matter distribution. The MCPM density field also generates a qualitatively similar cosmic web reconstruction as the DTFE density field from DM particles. Hence, our new method leveraging the MCPM density field from galaxy tracers to identify filaments in DISPERSE is potentially very powerful, as cosmic web reconstructions with a level of fidelity similar to that using DM particle tracers can be achieved. This has substantial implications for identifying filaments from any observed galaxy catalog (see section 4.4).

4.2. So How Do Filaments Affect Star Formation and Gas Supply?

The new filament finding method using MCPM and DISPERSE that we introduced in this work reveals a wide range of filaments that the traditional DTFE-based method misses. This includes many low-persistence filaments in less dense regions of the universe than high-persistence filaments but are, nevertheless, diffuse bridges of matter connecting galaxies. Some authors have posited the existence of “tendrils” or thin filaments, which are small structures embedded within voids (Alpaslan et al. 2014; Crone Odekon et al. 2018; Porter et al. 2023). Most of these studies classify tendrils as intermediate density environments between filaments and voids, finding varying degrees of difference in the star formation activity and gas supply of these galaxies in these structures. Crone Odekon et al. (2018) showed that galaxies in the ALFALFA survey (Giovanelli et al. 2005) in tendrils are on average more massive but similar in color and HI gas fraction to those in voids, while filament galaxies are less gas-rich and redder. Similar results were reported for the GAMA survey (Driver et al. 2011) by Alpaslan et al. (2014).

The cosmic web filament catalogs we construct from the MCPM density fields reveal a population of tendril-like low-persistence filaments. When considering the distance of galaxies to all filaments identified by our new method, there is generally very little dependence of galactic star formation or gas fraction on this distance – a consequence of the fact that most galaxies live within ~ 2.5 Mpc from a filament. However, there is a very notable dependence of galactic properties on the characteristic 1D filament line density we define. Interpreting galaxies living in low-line density filaments as tendrils, we see that these are the galaxies with highest star formation activity and gas fraction at any given mass and redshift (Figs. 11 and 14), consistent with the results of Crone Odekon et al. (2018) and Alpaslan et al. (2014). Therefore, a key result of our work is the discovery of a *differential effect* of filaments based on their line density; galaxies have less gas and star formation in thicker or higher line density filaments, but galaxies are the most gas-rich and star-forming in lower line density or thin filaments.

Our approach of quantifying filament line density using the MCPM density field information addresses the issue of point set estimates in DISPERSE. Otherwise, there is only topological information about the critical points of the density field. Therefore, filaments are represented as lines of infinitesimal width without information on the physical filament-to-filament diversity. We showed that persistence correlates with our estimated Σ_{fil} (MCPM), verifying our hypothesis that the higher the average persistence of a filament, the higher the line density of the filament. However, persistence is a single value provided on a per-filament-segment basis, where the MCPM density is an effective proxy for DM density and is defined for all points in the volume. Zhu et al. (2022) reconstructed the cosmic web using a Hessian-based method in a cosmological simulation run with the adaptive mesh refinement (AMR) code RAMSES (Teyssier 2002)

and studied the gas accretion rates in DM halos residing in tenuous/thin (with diameters $< 3 \text{ Mpc } h^{-1}$) and prominent/thick (with diameters $> 3 \text{ Mpc } h^{-1}$) filaments. They found that the gas accretion rate to $\log(M_{200,c}/M_{\odot}) < 12$ halos is noticeably lower when they reside in thicker filaments – by $\approx 20\text{-}30\%$ at $z = 0.5$ and $\approx 200\text{-}300\%$ at $z = 0$. At higher z , they found no significant differences in gas accretion rates between thin and thick filaments at higher z and larger halo masses. They also reported a minimal dependence of the gas accretion rate on the distance from the filament spine to the halo center. Although we measured filament “widths” in a different way, our results are broadly consistent with theirs, since the availability of gas in the halo (f_{gas}) and star formation activity in the galaxy (sSFR) should generally follow from the rate at which gas accretes onto the halo. Namely, galaxies in thicker filaments have much lower gas fraction and star formation activity than those in thinner filaments, an effect that increases with time (decreasing redshift). Zhu et al. (2022) demonstrated that there is significantly more hot ($T > 10^6 \text{ K}$) gas in thicker filaments at lower redshift, which can result in the gas supply to galaxies, e.g., via cold accretion streams (Kereš et al. 2009), in these regions being cut off. Recently, Lu et al. (2023) identified quantified filamentary boundaries by the gas density profiles, baryon fraction, the existence of a shock, and virial equilibrium, all of which are consistent.

Numerous theoretical explorations have been made on the distribution of gas in cosmic web filaments at low redshift (e.g., Galárraga-Espinosa et al. 2021, 2022; Gouin et al. 2022) and high redshift (e.g., Mandelker et al. 2021; Ramsøy et al. 2021; Lu et al. 2023), whose results have far-reaching implications for the impact of filaments on galaxy formation. Using a cosmological zoom-in simulation run with the AREPO code as used in TNG, Lu et al. (2023) demonstrated that there are distinct radial zones, characterized by their own gas thermodynamic properties, in filaments at $z \sim 4$. They showed that filament cores contain cool, low-entropy gas shielded from the shock-heated exteriors, interpreting this zone as thin cold streams that are long believed to be the primary sources of feeding high- z galaxies (e.g., Dekel & Birnboim 2006; Dekel et al. 2009; Pichon et al. 2011). The high-resolution simulation of Liao & Gao (2019) run with the GADGET-3 code (Springel et al. 2005) showed that filaments can accelerate gas cooling and subsequent star formation inside halos at $z = 4$ and $z = 2.5$.

In this work, we found that the gas fraction and the star formation activity were at similar levels near and far from MCPM filaments and near thin and thick filaments at the early epochs of $z \geq 2$. This provides evidence that filaments at early times can efficiently supply gas into galaxies, which allows them to grow quickly. Our results suggest that even filaments of comparable line density (measured in terms of comoving filament segment length) are more effective in channeling gas into galaxies and fueling star formation at $z \gtrsim 2$ than at $z < 2$. Some authors, such as Birnboim et al. (2016), showed that filamentary condensation could occur for unstable filaments at early times, allowing the thin

streams mentioned above to feed halos with cold gas. If indeed cold cores are ubiquitous in filaments at high- z , regardless of the filament line density, then this would result in similar gas supply levels and subsequent star formation in galaxies located near almost all types of filament. This might naively be interpreted as a lack of filamentary dependence on gas supply and star formation at high- z . Still, we find evidence of star formation efficiency to vary with filamentary environments even at the highest redshifts we study. For instance, a noticeable decline in $\langle f_{\text{gas}} \rangle$ at the highest filament line density at $z = 2$ does not translate into a similar decline in $\langle \text{sSFR} \rangle$ at that line density. This implies an increased star-formation efficiency in thicker filaments in at least some galaxies at early times. Supporting this result is the finding in Ghodsi et al. (2023) from the SIMBA hydrodynamical simulations (Davé et al. 2019) that star formation efficiency (in their case defined as the sSFR divided molecular hydrogen mass) increases with redshift to $z = 4$ for the highest local galaxy densities, but that it has almost no redshift dependence for lower-density environments.

Regardless, a lack of strong dependence of star formation activity and/or galactic gas supply on environment (either defined with respect to the cosmic web or local overdensity) before the so-called “cosmic noon” of star formation activity (e.g., Madau & Dickinson 2014) is a result that has been corroborated by a plethora of observations (e.g., Darvish et al. 2016; Moutard et al. 2018; Momose et al. 2022) and simulations (e.g., Xu et al. 2020; Chang et al. 2022; Malavasi et al. 2022; Bulichi et al. 2023).

On the other hand, we do see a strong dependence of galactic phenomena on the cosmic web at later times. As filaments accrete matter from underdense voids, they grow in width, and the physical properties of gas evolve toward less hospitable conditions for cold gas supply and star formation. In a cosmological zoom-in simulation using RAMSES, Ramsøy et al. (2021) found that the filament gas density profile can be modeled as an isothermal cylinder with a core radius that closely tracks the size of the galaxy in which the filament ends, and which evolves as $\sim (1+z)^{-2.7}$. Interestingly, the functional form they use to model the gas density profile (their Eq. 4) is very similar to the best-fit model we use to describe the $\langle \text{sSFR} \rangle$ - Σ_{fil} (MCPM) relationship (Eq. 2), although with variable exponents. This likely has interesting implications for the physical mechanism connecting the gas density in filaments to the gas supply and star formation in galaxies. We wish to explore this using simple analytical models in future work.

Martizzi et al. (2019) found that in TNG100, in line with expectations from a long line of theoretical studies, there is a strong increase in the amount of hotter and denser gas in filaments from the high z to the local universe, gradually resulting in the formation of a pervasive Warm-hot Intergalactic Medium (WHIM; e.g., Davé et al. 2001; Cen & Ostriker 2006). With time, there is an increase, therefore, in physical mechanisms that can cut off the gas supply and/or quench galaxies living in thicker filaments. One such mechanism is the formation of accretion shocks at the boundaries of fila-

ments and other cosmic web structures, which can suppress gas accretion and ultimately quench galaxies at high- z (e.g., Pasha et al. 2022) and low- z (e.g., Zinger et al. 2018; Li et al. 2023). “Cosmic web stripping”, a form of ram pressure stripping of gas near filamentary cores, has been invoked by Benítez-Llambay et al. (2013) to explain how local dwarf satellites can lose their gas. This mechanism is in line with our finding in this work and in Paper I that satellites have strongly suppressed star formation and gas fraction at low z in dense cosmic environments. This is in contrast to the slow removal of gas, often referred to as “starvation” or “strangulation” which can cut off gas supply on relatively long timescales on the order of a Gyr (e.g., Larson et al. 1980; Peng et al. 2015).

Many of these processes are encapsulated by the “cosmic web detachment” model of Aragon Calvo et al. (2019), which explains the increase in quenching and decrease in gas content close to the cosmic web as a natural consequence of galaxies being detached from their primordial cold gas-supplying filaments at later times. In particular, our finding that satellites are strongly quenched in thicker filaments could be an effect of these galaxies being increasingly cut off from primordial filaments with time. We also note that it is also possible for galaxies to be “pre-processed” – i.e., experience environment-driven quenching – before accreting onto filaments (e.g., Fujita 2004; Liao & Gao 2019). While a detailed analysis of gas physical conditions such as temperature, density, and entropy is beyond the scope of this work, this is a topic we intend to explore to understand the physical connection between filamentary gas and galaxy formation at different epochs. We also aim to make predictions of directly measurable gas properties such as column density and kinematics as a function of filament line density and cosmic web environment in future work, which can be compared to QSO absorption spectroscopic observations.

In this work, we also quantified the relative effects of galaxy mass and filamentary environment on quenching galaxies in the local universe. We repeat an analysis similar to that of Peng et al. (2010) but using the density of the filament line as an environmental metric. We showed that Σ_{fil} (MCPM) is a highly effective quantity for assessing the environmental impact of the quenched or red fraction of galaxies. The segregation of $z < 0.1$ SDSS galaxies by red fraction was not shown to be so pronounced when using the MCPM density estimate directly Burchett et al. (see Figure 2 of 2020). At $z = 0$, $\log(M_*/M_\odot) \gtrsim 10.5$ galaxies are virtually all red ($g - r > 0.6$), regardless of the filament they live near or whether they are centrals or satellites. This is mostly a consequence of the black hole (BH) feedback model of TNG, where the growth of a central BH to mass $\log(M_{\text{BH}}/M_\odot) > 8.2$ results in a very rapid transition of the host galaxy to a quiescent state (Terrazas et al. 2020). The onset of a low-accretion “kinetic” mode of BH feedback consisting of a BH-driven wind in the TNG model is known to transform the thermodynamics of gas in the CGM and quench star formation in galaxies with $\log(M_*/M_\odot) \gtrsim 10.5$ (Zinger et al. 2020). This result does create some tension

with the observations (e.g., [Donnari et al. 2021](#)). However, AGN feedback is widely believed to be among the most important factors in quenching massive galaxies at any redshift (e.g., [Di Matteo et al. 2005](#); [Fabian 2012](#); [Somerville & Davé 2015](#)).

This is in line with the picture of *mass quenching* advocated by [Peng et al. \(2010\)](#) and others to show the dominant role that internal mechanisms such as stellar and AGN feedback play in regulating star formation in massive galaxies. At lower masses, however, the filamentary environment plays an important role in quenching galaxies. Thicker filaments have more quenched and red galaxies with $\log(M_*/M_\odot) < 10.5$ than thinner filaments. Like [Peng et al. \(2012\)](#), we find that this *environmental quenching* is dominated by satellite galaxies, albeit our work considers the global cosmic web environment rather than the local galaxy overdensity.

A crucial finding of this work is the apparent dependence of star formation efficiency on cosmic filaments. While satellite galaxies generally lose their gas supplies and become passive systems as they approach thicker filaments in later times, a different explanation is required for centrals at later times. High-mass low- z centrals experience a somewhat significant reduction in $\langle \text{sSFR} \rangle$, but do not have a similar reduction in $\langle f_{\text{gas}} \rangle$, in thicker filaments. Some physical mechanism(s) must be responsible for causing their star formation efficiency to decrease in these environments. One possible explanation is that the hydrodynamical conditions of gas in thicker filaments are inhospitable to star formation, for instance, due to higher temperatures and pressures, which prevent condensation and cooling to form stars. Alternatively, this could be mostly due to internal mechanisms such as AGN feedback, which can heat up gas in the CGM and prevent star formation as a result (e.g., [Voit et al. 2015](#); [Donahue & Voit 2022](#)). We defer a detailed analysis of the cosmic web dependence of BH mass and/or accretion phenomena to future work.

Finally, we make some remarks about numerical and modeling considerations in interpreting our results on the galaxy-cosmic web connection. One such consideration is the impact of feedback in the gas fraction and star formation of galaxies. [Davé et al. \(2020\)](#) compared the gas in various cosmological simulations with different subgrid prescriptions and numerical methods. They found that despite broad agreement between different simulation suites in global statistical distributions and scaling relations (such as the gas to stellar mass relation), there are quantitative differences with galaxy properties. The differing model of AGN and supernovae (SNe) feedback between TNG and EAGLE, for example, causes much lower HI gas fraction in low-mass galaxies in EAGLE. However, TNG is also known to somewhat overproduce gas fractions in massive galaxies relative to observations (e.g., [Diemer et al. 2019](#); [Stevens et al. 2019](#)). Numerical resolution is also a source of uncertainty which will no doubt affect the gas supply, and ultimately quenching, of galaxies (e.g., [Pillepich et al. 2019](#); [Nelson et al. 2020](#)). Lastly, the baryonic mass resolution of $\sim 1.4 \times 10^6 M_\odot$ in TNG100 means that the lowest mass galaxies

we study, i.e. $\log(M_*/M_\odot) \approx 8$, might not be very well-resolved, and therefore the statistics of low-mass galaxies ($8 \leq \log(M_*/M_\odot) < 9$) carry some numerical uncertainty.

4.3. Effect of Local Environment

We have alluded to the potential effect of local environment in shaping the dependence of galactic properties on the cosmic web. Here, we attempt to understand whether the effect of the cosmic web on star formation and gas fraction persists when controlling for two local environmental variables, MCPM overdensity ($1 + \delta_\rho$ (MCPM), measured at the location of a galaxy) and halo mass ($M_{200,c}$). We measure $\langle \text{sSFR} \rangle$ and $\langle f_{\text{gas}} \rangle$ in bins of z and M_* as before, but keep $1 + \delta_\rho$ (MCPM) and $M_{200,c}$ fixed. First, we perform these measurements only by considering galaxies within the middle 1/3 (33%-66%) of the $1 + \delta_\rho$ (MCPM) distribution for a given z . The resulting $\langle \text{sSFR} \rangle$ - Σ_{fil} (MCPM) and $\langle f_{\text{gas}} \rangle$ - Σ_{fil} (MCPM) relationships are shown in the top two rows of [Figure 15](#). After controlling for local overdensity (recall that this is smoothed on scales of ~ 0.5 Mpc), the effect of filament line density on star formation and gas supply still persists. In particular, at $z \leq 0.5$, there is a clear reduction in star formation activity and the gas fraction of galaxies of all masses with Σ_{fil} (MCPM) after controlling for local overdensity, albeit the effect is lessened from the case where no overdensity cut was imposed ([Figures 11 and 14](#)). This indicates that while *some* of the quenching and reduction of gas is caused by high local density, there is still a residual effect of the cosmic web on these phenomena. We note that changing the control $1 + \delta_\rho$ (MCPM) range somewhat (say, from the middle 1/3 to the middle 1/2 of the distribution) does not qualitatively affect this conclusion above.

Next, we repeat our measurements but keeping $M_{200,c}$ fixed. We set a maximum halo mass of $\log(M_{200,c}/M_\odot) = 13.5$ only to consider galaxies that do not reside in massive groups or clusters, which all belong to nodes of the cosmic web (CP_{max} ; [Section 2.5](#)). The resulting $\langle \text{sSFR} \rangle$ - Σ_{fil} (MCPM) and $\langle f_{\text{gas}} \rangle$ - Σ_{fil} (MCPM) relationships are shown in the bottom two rows of [Figure 15](#). Similarly to keeping $1 + \delta_\rho$ (MCPM) fixed, we find that the effect of Σ_{fil} (MCPM) on galaxies persists after keeping $M_{200,c}$ fixed. While the effect of the most massive halos is significant in shaping the star formation and gas supply of galaxies, there is an effect of filament line density *beyond* halo mass. However, we note that reducing the halo mass threshold above reduces the effect of Σ_{fil} (MCPM) on $\langle \text{sSFR} \rangle$ and f_{gas} , implying that smaller halos can still play an important role in regulating gas supply and quenching.

Recently, [Wang et al. \(2023\)](#) used DISPERSE to establish the effect of the cosmic web environment on galaxies beyond the halo mass, finding that halos of fixed mass near nodes and filaments have more galaxies than those halos further away. They stressed the importance of removing host-halo effects by considering similar halo mass distributions to isolate the effects of the environment on galaxies. Furthermore, several past studies have shown that the environmental dependence of galaxies may originate from the corresponding

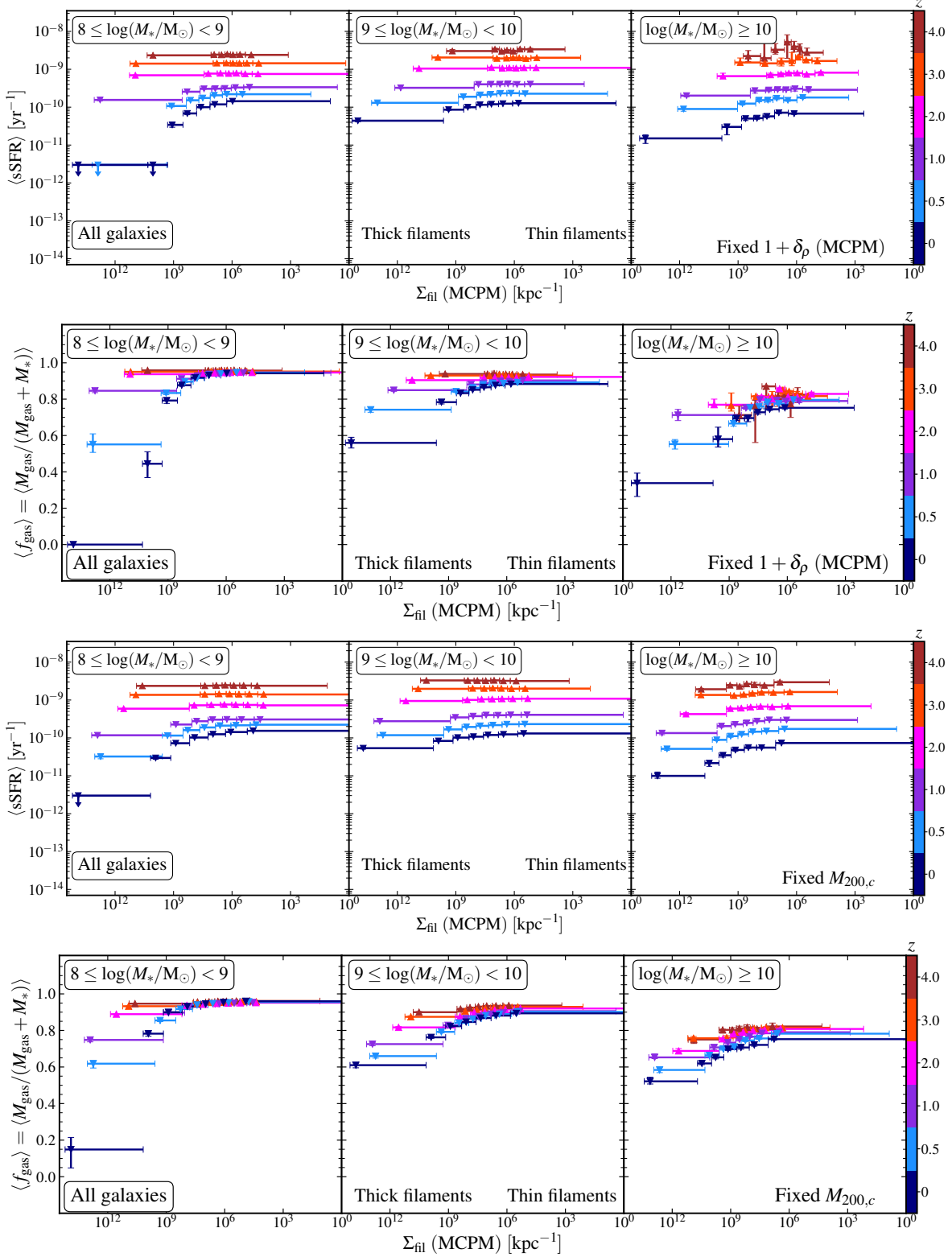


Figure 15. The effect of filament line density on star formation and gas fraction after controlling for local environmental effects. The top two rows show $\langle sSFR \rangle$ vs. Σ_{fil} (MCPCP) and $\langle f_{gas} \rangle$ vs. Σ_{fil} (MCPCP), respectively, for a fixed MCPCP overdensity, while the bottom two rows show these relationships for a fixed halo mass (see text). The effect of filament line density on star formation and gas fraction persists after local environment is taken into account.

environmental dependence of the host halo mass or that the growth of halos drives the measured properties of galaxies (e.g., [Dragomir et al. 2018](#); [Donnan et al. 2022](#); [Scholz-Díaz et al. 2023](#)).

Interestingly enough, there appears to be a much stronger dependence of the gas fraction than star formation activity on the filaments after accounting for the local environment. This effect, especially pronounced for low- z $\log(M_*/M_\odot) \geq 10$ galaxies, potentially indicates that the cosmic web environment impacts the efficiency with which gas is converted to stars beyond the local environment. This aligns with several other lines of evidence in this paper, which showed a differential star formation efficiency in different cosmic web environments. Finally, we remark that the local environment will inevitably be linked to the global cosmic web environment, as more massive halos and regions of higher local density will be in nodes and thicker filaments. Hence, disentangling the effect of local density from that of filaments is not trivial.

4.4. Application to Observations

We have demonstrated that this new cosmic web filament-finding methodology can be applied to any catalog of galaxies to extract highly detailed information on the characteristics of filaments and their effect on galaxy evolution. We are conducting an archival research program for Cycle 31 *Hubble Space Telescope* (HST) (AR# 17568; PI: Hasan) to apply this method to observed galaxy catalogs from SDSS. From a catalog of $\sim 600,000$ galaxies in SDSS, MCPM density fields were constructed to $z \simeq 0.5$ by [Wilde et al. \(2023\)](#). We will apply these density fields as input to DISPERSE to reconstruct the cosmic web structure out to $\approx 40\%$ the age of the universe and identify filaments with greater fidelity than ever before in the real universe. The application to real galaxy catalogs will be done in redshift space instead of Cartesian space as in the simulation application in this paper, which includes redshift space distortions and peculiar velocities (e.g., [Kaiser 1984](#)). In future work, we will test our method in mock redshift space in simulations.

For our HST program, we will probe the filaments identified in the SDSS volume with absorption features in the spectra of background QSOs, observed with the Cosmic Origins Spectrograph (COS) onboard HST ([Green et al. 2012](#)), allowing detailed studies of the gas in different cosmic web environments using the tried-and-tested method of QSO absorption spectroscopy (e.g., [Bordoloi et al. 2014](#); [Burchett et al. 2016](#); [Hasan et al. 2020](#)). We will use commonly observed absorption features such as Ly α and OVI in existing archival HST/COS QSO spectra to place unprecedented constraints on the gas in cosmic web filaments and how this affects the baryon cycle (e.g., [Tumlinson et al. 2017](#); [Péroux & Howk 2020](#)) that regulates galaxy evolution. Therefore, our work will go a long way in ascertaining the importance of the physical conditions of filamentary gas in the supply and quenching of galactic gas.

Beyond this archival program, we expect to apply our method to other state-of-the-art observational surveys of galaxies at even higher redshifts. Large surveys with sky cov-

erage similar to SDSS from the Dark Energy Spectroscopic Instrument (DESI), particularly the Luminous Red Galaxies (LRGs) and Emission Line Galaxies (ELGs) (see [Lan et al. 2023](#), and references therein), will allow the identification of cosmic web filaments out to $z \simeq 1.6$. The Subaru Prime Focus Spectrograph (PFS; [Takada et al. 2014](#)) will also be extremely valuable in this enterprise, as the PFS Galaxy Evolution program will observe up to half a million galaxies at redshifts $0.7 \lesssim z \lesssim 7$, including a deep survey of $> 10^5$ continuum-selected galaxies out to $z \sim 2$ ([Greene et al. 2022](#)). In addition, the Euclid Wide Survey ([Euclid Collaboration et al. 2022](#)) and the SPHEREx All-sky Survey ([Doré et al. 2016](#)) will provide the large galaxy catalogs needed to reconstruct the cosmic web over most of cosmic time. Such datasets will enable us to identify filaments from MCPM cosmic density fields at the peak epoch of star formation activity and test our predictions of a lack of cosmic web dependence of quenching and gas supply of galaxies in the first ≈ 4 Gyr of the universe.

Additionally, the *James Webb Space Telescope* (JWST), thanks to programs such as JADES ([Cameron et al. 2023](#)), will provide galaxy spectra at the epoch of cosmic dawn ($z \gtrsim 4$) over much smaller fields of view. This will allow us to generate limited cosmic web reconstructions in the first ~ 1 Gyr of the universe. Ultimately, our filament finding method can be applied to galaxy catalogs observed by the Roman Space Telescope, especially the planned High Latitude Wide Area Survey, which will observe millions of galaxies up to $z \sim 3$ ([Wang et al. 2022](#)).

5. CONCLUSIONS

In our study, we used the DISPERSE algorithm to identify filaments in the cosmic web structure of the TNG100 simulations at redshifts $z = 0, 0.5, 1, 2, 3$, and 4. We analyzed the output filamentary structure and its impact on galaxy evolution using two different density field estimates, the prepackaged DTFE density field ([Schaap & van de Weygaert 2000](#)) and the MCPM density field inspired by slime mold ([Burchett et al. 2020](#)). Our findings are summarized below.

1. DISPERSE is more accurate in identifying filaments when using the MCPM density field than the DTFE density field. Filaments identified by the MCPM method are more numerous, have more natural shapes, and provide a more accurate representation of the cosmic mass and galaxy distribution than those identified by the DTFE method. Additionally, the MCPM method can identify lower-density, less prominent filaments that the DTFE method misses.
2. Most galaxies are located within a distance of approximately $\sim 1.5 - 2.5$ Mpc from the spine of an MCPM filament. On the other hand, many galaxies are far away from DTFE filaments. As a result, the median sSFR $\langle \text{sSFR} \rangle$ and the median gas fraction $\langle f_{\text{gas}} \rangle$ show minimal dependency on the distance to the filament spine when MCPM filaments are taken into account, unlike in the case of DTFE filaments.

3. We define the line density of filaments, denoted Σ_{fil} (MCPM), as the total MCPM overdensity per unit length of a filament segment. At low redshifts ($z \leq 1$), star formation is suppressed in galaxies near high-line density or ‘thick’ filaments. However, the correlation is almost non-existent at higher redshifts ($z > 2$). Thick filaments strongly quench satellites of all masses, while high-mass (in the range of $\log(M_*/M_\odot) \geq 10$) centrals have lower star formation in these environments at lower redshifts.
4. At a redshift of $z = 0$, we find that the red fraction of galaxies ($g - r > 0.6$) and the fraction of galaxies that have been quenched ($\log(\text{sSFR}/\text{yr}^{-1}) < -11$) are not affected by their environment when their stellar mass is above $\log(M_*/M_\odot) > 10.5$. However, at lower masses, galaxies tend to be redder and more likely to be quenched when the filament line density is higher for a given galaxy mass. Additionally, satellites are more susceptible to the effects of the filamentary environment than central galaxies.
5. We conclude that the line density of filaments plays a significant role in forming stars via the gas supply available to galaxies. This relationship can be attributed to the amount of gas present in galaxies: galaxies with a higher gas fraction tend to form stars more frequently in areas with a denser filament. Galaxies in thicker filaments lose their gas, especially at lower redshifts. This pattern continues to redshifts of $z = 4$.
6. We also find that the efficiency of star formation appears to vary depending on the filamentary environment, especially at later times. The effect of filament line density on satellite galaxies at low- z is fairly straightforward: thicker filaments cut off the gas supply and quench satellites. However, the story is more complicated for late-time centrals, as these are, to some extent, quenched near thick filaments despite no corresponding reduction of their gas reservoirs.

Our scientific results point to a picture in which thicker filaments of the cosmic web act to reduce the gas supply and star formation activity of galaxies the last ~ 10 Gyr of cosmic time. Physical mechanisms such as ram pressure stripping from filament cores or accretion shock-heating from filament outskirts could be responsible for such effects, essentially disconnecting galaxies (mostly satellites) from their primordial cold gas supply, leading to starvation and then quenching. Central galaxies feel the effect of filaments the least. However, they do exhibit lower star formation and lower star formation efficiency in thicker filaments at later times, which could be explained by the hydrodynamical effects of gas in these filaments suppressing star formation or perhaps as an internal effect from AGN feedback in these galaxies. We showed that the filamentary dependence of these galaxy formation phenomena persists after accounting for the effect of the local environment. In the early universe, thin, narrow

streams could efficiently feed galaxies even in thicker filaments, allowing high levels of star formation activity ubiquitously throughout the universe.

We showed how well DISPERSE does in identifying filaments with the powerful MCPM density field, and we presented a fairly simple procedure to calibrate the persistence parameter to match physical expectations of large-scale structure, similar to Galárraga-Espinosa et al. (2023). We hope that our work will be the first of many to take advantage of this density estimation method to identify filaments of the cosmic web. Similar reconstructions can be easily performed on other hydrodynamical cosmological simulations such as EAGLE (Schaye et al. 2015), SIMBA (Davé et al. 2019), Romulus (Tremmel et al. 2017), Magneticum (Dolag et al. 2016), FIREbox (Feldmann et al. 2023), and NewHorizon (Dubois et al. 2021), as well as different resolution and volume runs of the TNG project, including TNG50 (Pillepich et al. 2019; Nelson et al. 2020) and MilleniumTNG (Pakmor et al. 2023). Comparisons between these simulations and the results in TNG100 we presented here will yield important insights into how subgrid physics, stellar/AGN feedback, numerical resolution, etc. affect the properties of large-scale structures and their interplay with galaxies.

Perhaps even more exciting is that our new method can be applied to observational datasets to identify the cosmic web structure in the real universe. With rich datasets of galaxy catalogs from state-of-the-art current and upcoming observatories such as SDSS, DESI, Subaru PFS, JWST, Euclid, SPHEREx, and Roman, we will be in a position to identify filaments with high fidelity across most of cosmic time. This has the potential to unlock a rich array of investigations in a plethora of research areas of extragalactic astrophysics and cosmology. Among the myriad possibilities offered by MCPM and its improved filament finding are (1) the accurate characterization of cosmic voids to constrain cosmological parameters (e.g., Pisani et al. 2015), (2) a detailed mapping of the intergalactic medium (IGM) and finding of the so-called “missing baryons” of the universe (e.g., Shull et al. 2012; Nicastro et al. 2018), and (3) localization of transient phenomena such as gravitational waves and fast radio bursts (e.g., CHIME/FRB Collaboration et al. 2020; Agazie et al. 2023).

DATA AVAILABILITY

The catalogs used in this work are available at <https://github.com/farhantasy/CosmicWeb-Galaxies/>. Please cite this paper if you wish to use any of the data.

1 The authors are grateful to N. Lubber and Z. Edwards for
 2 their help setting up DISPERSE. We thank participants of
 3 the 2023 Santa Cruz Galaxy Workshop for insightful discus-
 4 sions. We also acknowledge stimulating discussions with V.
 5 Pandya, H. Aung, H. Zhang, J. Powell, C. Cadiou, L. Scholz-
 6 Díaz, S. Simha, K-G. Lee, R. Momose, F. van den Bosch,
 7 N. Gluck, C. Pichon, U. Kuchner, C. Welker, M. Strauss,
 8 R. Dave, J. Greene, R. Teyssier, N. Lubber, J. van Gorkom,
 9 X. Wang, B. Frye, S. Juneau, S. Alberts, S. Tonnesen, L.
 10 Sales, D. French, J. Tumlinson, J. Wu, P. Mansfield, K. Fin-
 11 lator, A. Coil, S. Alberts. This research used resources of
 12 the National Energy Research Scientific Computing Center, a
 13 DOE Office of Science User Facility supported by the Office
 14 of Science of the US Department of Energy under Contract
 15 No. DE-AC02-05CH11231 using the NERSC award HEP-
 16 ERCAP0024028. FH and JNB are supported by the National
 17 Science Foundation LEAPS-MPS award #2137452. OE is
 18 supported by an incubator fellowship from the Open Source
 19 Program Office at UC Santa Cruz funded by the Alfred P.
 20 Sloan Foundation (G-2021-16957). DN is supported by NSF
 21 (AST-2206055 & 2307280) and NASA (80NSSC22K0821 &
 22 TM3-24007X) grants. NM acknowledges support from the
 23 Israel Science Foundation (ISF) grant 3061/21 and US-Israel
 24 Binational Science Foundation (BSF) grant 2020302.

REFERENCES

- Adamatzky, A. 2010, *Physarum Machines: Computers from Slime Mould*, World Scientific series on nonlinear science (World Scientific)
- Adamatzky, A., Armstrong, R., Jones, J., & Gunji, Y.-P. 2013, *International Journal of General Systems*, 42, 441-457
- Agazie, G., Anumarlapudi, A., Archibald, A. M., et al. 2023, *ApJL*, 951, L8
- Alam, S., Zu, Y., Peacock, J. A., & Mandelbaum, R. 2019, *MNRAS*, 483, 4501
- Alpaslan, M., Robotham, A. S. G., Driver, S., et al. 2014, *MNRAS*, 438, 177
- Aragon Calvo, M. A., Neyrinck, M. C., & Silk, J. 2019, *The Open Journal of Astrophysics*, 2, 7
- Aragón-Calvo, M. A., Platen, E., van de Weygaert, R., & Szalay, A. S. 2010, *ApJ*, 723, 364
- Baldry, I. K., Balogh, M. L., Bower, R. G., et al. 2006, *MNRAS*, 373, 469
- Balogh, M. L., Morris, S. L., Yee, H. K. C., Carlberg, R. G., & Ellingson, E. 1999, *ApJ*, 527, 54
- Behroozi, P. S., Wechsler, R. H., & Conroy, C. 2013, *ApJ*, 770, 57
- Benítez-Llambay, A., Navarro, J. F., Abadi, M. G., et al. 2013, *ApJL*, 763, L41
- Birnbom, Y., Padnos, D., & Zinger, E. 2016, *ApJL*, 832, L4
- Blanton, M. R., Eisenstein, D., Hogg, D. W., Schlegel, D. J., & Brinkmann, J. 2005, *ApJ*, 629, 143
- Bluck, A. F. L., Maiolino, R., Sánchez, S. F., et al. 2020, *MNRAS*, 492, 96
- Blue Bird, J., Davis, J., Lubber, N., et al. 2020, *MNRAS*, 492, 153
- Bond, J. R., Kofman, L., & Pogosyan, D. 1996, *Nature*, 380, 603
- Bonjean, V., Aghanim, N., Douspis, M., Malavasi, N., & Tanimura, H. 2020, *A&A*, 638, A75
- Bordoloi, R., Tumlinson, J., Werk, J. K., et al. 2014, *ApJ*, 796, 136
- Brown, T., Catinella, B., Cortese, L., et al. 2017, *MNRAS*, 466, 1275
- Bryant, J. J., Owers, M. S., Robotham, A. S. G., et al. 2015, *MNRAS*, 447, 2857
- Bulich, T.-E., Dave, R., & Kraljic, K. 2023, *arXiv e-prints*, arXiv:2309.03282
- Burchett, J. N., Elek, O., Tejos, N., et al. 2020, *ApJL*, 891, L35
- Burchett, J. N., Tripp, T. M., Bordoloi, R., et al. 2016, *ApJ*, 832, 124
- Cameron, A. J., Saxena, A., Bunker, A. J., et al. 2023, *arXiv e-prints*, arXiv:2302.04298
- Cautun, M., van de Weygaert, R., & Jones, B. J. T. 2013, *MNRAS*, 429, 1286
- Cautun, M., van de Weygaert, R., Jones, B. J. T., & Frenk, C. S. 2014, *MNRAS*, 441, 2923
- Cavaliere, A., & Fusco-Femiano, R. 1978, *A&A*, 70, 677
- Cen, R., & Ostriker, J. P. 2006, *ApJ*, 650, 560
- Chang, W., Fang, G., Gu, Y., et al. 2022, *ApJ*, 936, 47

- CHIME/FRB Collaboration, Andersen, B. C., Bandura, K. M., et al. 2020, *Nature*, **587**, 54
- Codis, S., Jindal, A., Chisari, N. E., et al. 2018, *MNRAS*, **481**, 4753
- Codis, S., Pichon, C., Devriendt, J., et al. 2012, *MNRAS*, **427**, 3320
- Cohn, J. D. 2022, *MNRAS*, **513**, 624
- Colless, M., Dalton, G., Maddox, S., et al. 2001, *MNRAS*, **328**, 1039
- Crone Odekon, M., Hallenbeck, G., Haynes, M. P., et al. 2018, *ApJ*, **852**, 142
- Darvish, B., Mobasher, B., Sobral, D., et al. 2016, *ApJ*, **825**, 113
- Darvish, B., Sobral, D., Mobasher, B., et al. 2014, *ApJ*, **796**, 51
- Davé, Romeel, A. D., Narayanan, D., Li, Q., Rafieferantsoa, M. H., & Appleby, S. 2019, *MNRAS*, **486**, 2827
- Davé, R., Crain, R. A., Stevens, A. R. H., et al. 2020, *MNRAS*, **497**, 146
- Davé, R., Cen, R., Ostriker, J. P., et al. 2001, *ApJ*, **552**, 473
- Davidzon, I., Cucciati, O., Bolzonella, M., et al. 2016, *A&A*, **586**, A23
- de Lapparent, V., Geller, M. J., & Huchra, J. P. 1986, *ApJL*, **302**, L1
- De Lucia, G., Poggianti, B. M., Aragón-Salamanca, A., et al. 2007, *MNRAS*, **374**, 809
- Dekel, A., & Birnboim, Y. 2006, *MNRAS*, **368**, 2
- Dekel, A., Birnboim, Y., Engel, G., et al. 2009, *Nature*, **457**, 451
- Di Matteo, T., Springel, V., & Hernquist, L. 2005, *Nature*, **433**, 604
- Diemer, B., Stevens, A. R. H., Lagos, C. d. P., et al. 2019, *MNRAS*, **487**, 1529
- Dolag, K., Borgani, S., Murante, G., & Springel, V. 2009, *MNRAS*, **399**, 497
- Dolag, K., Komatsu, E., & Sunyaev, R. 2016, *MNRAS*, **463**, 1797
- Donahue, M., & Voit, G. M. 2022, *PhR*, **973**, 1
- Donnan, C. T., Tojeiro, R., & Kraljic, K. 2022, *Nature Astronomy*, **6**, 599
- Donnari, M., Pillepich, A., Nelson, D., et al. 2021, *MNRAS*, **506**, 4760
- Doré, O., Werner, M. W., Ashby, M., et al. 2016, *arXiv e-prints*, [arXiv:1606.07039](https://arxiv.org/abs/1606.07039)
- Dragomir, R., Rodríguez-Puebla, A., Primack, J. R., & Lee, C. T. 2018, *MNRAS*, **476**, 741
- Dressler, A. 1980, *ApJ*, **236**, 351
- Driver, S. P., Hill, D. T., Kelvin, L. S., et al. 2011, *MNRAS*, **413**, 971
- Dubois, Y., Pichon, C., Welker, C., et al. 2014, *MNRAS*, **444**, 1453
- Dubois, Y., Beckmann, R., Bournaud, F., et al. 2021, *A&A*, **651**, A109
- Einasto, J. 1965, *Trudy Astrofizicheskogo Instituta Alma-Ata*, **5**, 87
- Elbaz, D., Daddi, E., Le Borgne, D., et al. 2007, *A&A*, **468**, 33
- Elek, O., Burchett, J. N., Prochaska, J. X., & Forbes, A. G. 2021, *IEEE Transactions on Visualization and Computer Graphics*, **27**, 806-816
- . 2022, *Artificial Life*, 28
- Euclid Collaboration, Scaramella, R., Amiaux, J., et al. 2022, *A&A*, **662**, A112
- Faber, S. M., Willmer, C. N. A., Wolf, C., et al. 2007, *ApJ*, **665**, 265
- Fabian, A. C. 2012, *ARA&A*, **50**, 455
- Falck, B. L., Neyrinck, M. C., & Szalay, A. S. 2012, *ApJ*, **754**, 126
- Feldmann, R., Quataert, E., Faucher-Giguère, C.-A., et al. 2023, *MNRAS*, **522**, 3831
- Fujita, Y. 2004, *PASJ*, **56**, 29
- Galárraga-Espinosa, D., Aghanim, N., Langer, M., & Tanimura, H. 2021, *A&A*, **649**, A117
- Galárraga-Espinosa, D., Langer, M., & Aghanim, N. 2022, *A&A*, **661**, A115
- Galárraga-Espinosa, D., Cadiou, C., Gouin, C., et al. 2023, *arXiv e-prints*, [arXiv:2309.08659](https://arxiv.org/abs/2309.08659)
- Ganeshaiah Veena, P., Cautun, M., Tempel, E., van de Weygaert, R., & Frenk, C. S. 2019, *MNRAS*, **487**, 1607
- Geller, M. J., & Huchra, J. P. 1989, *Science*, **246**, 897
- Ghods, L., Man, A., Donevski, D., et al. 2023, *arXiv e-prints*, [arXiv:2309.01277](https://arxiv.org/abs/2309.01277)
- Giovanelli, R., Haynes, M. P., Kent, B. R., et al. 2005, *AJ*, **130**, 2598
- Gouin, C., Gallo, S., & Aghanim, N. 2022, *A&A*, **664**, A198
- Green, J. C., Froning, C. S., Osterman, S., et al. 2012, *ApJ*, **744**, 60
- Greene, J., Bezanson, R., Ouchi, M., Silverman, J., & the PFS Galaxy Evolution Working Group. 2022, *arXiv e-prints*, [arXiv:2206.14908](https://arxiv.org/abs/2206.14908)
- Hasan, F., Churchill, C. W., Stemmock, B., et al. 2020, *ApJ*, **904**, 44
- Hasan, F., Burchett, J. N., Abeyta, A., et al. 2023, *ApJ*, **950**, 114
- Huchra, J. P., Macri, L. M., Masters, K. L., et al. 2012, *ApJS*, **199**, 26
- Ilbert, O., McCracken, H. J., Le Fèvre, O., et al. 2013, *A&A*, **556**, A55
- Janowiecki, S., Catinella, B., Cortese, L., et al. 2017, *MNRAS*, **466**, 4795
- Jones, J. 2010, *Artificial Life*, **16**, 127-153
- Kaiser, N. 1984, *ApJL*, **284**, L9
- Kauffmann, G., White, S. D. M., Heckman, T. M., et al. 2004, *MNRAS*, **353**, 713
- Kereš, D., Katz, N., Fardal, M., Davé, R., & Weinberg, D. H. 2009, *MNRAS*, **395**, 160
- Kleiner, D., Pimblet, K. A., Jones, D. H., Koribalski, B. S., & Serra, P. 2017, *MNRAS*, **466**, 4692
- Klypin, A., Yepes, G., Gottlöber, S., Prada, F., & Heß, S. 2016, *MNRAS*, **457**, 4340
- Kotecha, S., Welker, C., Zhou, Z., et al. 2022, *MNRAS*, **512**, 926

- Kraljic, K., Duckworth, C., Tojeiro, R., et al. 2021, *MNRAS*, 504, 4626
- Kraljic, K., Arnouts, S., Pichon, C., et al. 2018, *MNRAS*, 474, 547
- Kraljic, K., Pichon, C., Dubois, Y., et al. 2019, *MNRAS*, 483, 3227
- Kuchner, U., Aragón-Salamanca, A., Pearce, F. R., et al. 2020, *MNRAS*, 494, 5473
- Kuutma, T., Tamm, A., & Tempel, E. 2017, *A&A*, 600, L6
- Laigle, C., McCracken, H. J., Ilbert, O., et al. 2016, *ApJS*, 224, 24
- Laigle, C., Pichon, C., Arnouts, S., et al. 2018, *MNRAS*, 474, 5437
- Lan, T.-W., Tojeiro, R., Armengaud, E., et al. 2023, *ApJ*, 943, 68
- Larson, R. B., Tinsley, B. M., & Caldwell, C. N. 1980, *ApJ*, 237, 692
- Li, H., Wang, H., Mo, H. J., et al. 2023, *ApJ*, 942, 44
- Liao, S., & Gao, L. 2019, *MNRAS*, 485, 464
- Libeskind, N. I., van de Weygaert, R., Cautun, M., et al. 2018, *MNRAS*, 473, 1195
- Lilly, S. J., Le Fèvre, O., Renzini, A., et al. 2007, *ApJS*, 172, 70
- Lu, Y. S., Mandelker, N., Oh, S. P., et al. 2023, *arXiv e-prints*, [arXiv:2306.03966](https://arxiv.org/abs/2306.03966)
- Madau, P., & Dickinson, M. 2014, *ARA&A*, 52, 415
- Malavasi, N., Langer, M., Aghanim, N., Galárraga-Espinosa, D., & Gouin, C. 2022, *A&A*, 658, A113
- Mandelker, N., van den Bosch, F. C., Springel, V., et al. 2021, *ApJ*, 923, 115
- Martizzi, D., Vogelsberger, M., Artale, M. C., et al. 2019, *MNRAS*, 486, 3766
- Momose, R., Lee, K.-G., Horowitz, B., Ata, M., & Kartaltepe, J. S. 2022, *arXiv e-prints*, [arXiv:2212.05984](https://arxiv.org/abs/2212.05984)
- Moore, B., Katz, N., Lake, G., Dressler, A., & Oemler, A. 1996, *Nature*, 379, 613
- Moorman, C. M., Vogeley, M. S., Hoyle, F., et al. 2014, *MNRAS*, 444, 3559
- Moutard, T., Sawicki, M., Arnouts, S., et al. 2018, *MNRAS*, 479, 2147
- Nagai, D., Kravtsov, A. V., & Vikhlinin, A. 2007, *ApJ*, 668, 1
- Nakagaki, T., Yamada, H., & Tóth, Á. 2000, *Nature*, 407, 470
- Nelson, D., Pillepich, A., Springel, V., et al. 2018, *MNRAS*, 475, 624
- Nelson, D., Springel, V., Pillepich, A., et al. 2019, *Computational Astrophysics and Cosmology*, 6, 2
- Nelson, D., Sharma, P., Pillepich, A., et al. 2020, *MNRAS*, 498, 2391
- Nicastro, F., Kaastra, J., Krongold, Y., et al. 2018, *Nature*, 558, 406
- Pakmor, R., Springel, V., Coles, J. P., et al. 2023, *MNRAS*, 524, 2539
- Pandya, V., Primack, J., Behroozi, P., et al. 2019, *MNRAS*, 488, 5580
- Pasha, I., Mandelker, N., van den Bosch, F. C., Springel, V., & van de Voort, F. 2022, *MNRAS*
- Peng, Y.-j., Lilly, S. J., Renzini, A., & Carollo, M. 2012, *ApJ*, 757, 4
- Peng, Y.-j., Lilly, S. J., Kovač, K., et al. 2010, *ApJ*, 721, 193
- Péroux, C., & Howk, J. C. 2020, *ARA&A*, 58, 363
- Pichon, C., Pogosyan, D., Kimm, T., et al. 2011, *MNRAS*, 418, 2493
- Pillepich, A., Springel, V., Nelson, D., et al. 2018, *MNRAS*, 473, 4077
- Pillepich, A., Nelson, D., Springel, V., et al. 2019, *MNRAS*, 490, 3196
- Pisani, A., Sutter, P. M., Hamaus, N., et al. 2015, *PhRvD*, 92, 083531
- Planck Collaboration, Ade, P. A. R., Aghanim, N., et al. 2016, *A&A*, 594, A13
- Poggianti, B. M., von der Linden, A., De Lucia, G., et al. 2006, *ApJ*, 642, 188
- Porter, L. E., Holwerda, B. W., Kruk, S., et al. 2023, *MNRAS*, 524, 5768
- Ramsøy, M., Slyz, A., Devriendt, J., Laigle, C., & Dubois, Y. 2021, *MNRAS*, 502, 351
- Rosas-Guevara, Y., Tissera, P., Lagos, C. d. P., Paillas, E., & Padilla, N. 2022, *MNRAS*, 517, 712
- Rost, A., Staszczyn, F., Pereyra, L., & Martínez, H. J. 2020, *MNRAS*, 493, 1936
- Schaap, W. E., & van de Weygaert, R. 2000, *A&A*, 363, L29
- Schawinski, K., Urry, C. M., Simmons, B. D., et al. 2014, *MNRAS*, 440, 889
- Schaye, J., Crain, R. A., Bower, R. G., et al. 2015, *MNRAS*, 446, 521
- Scholz-Díaz, L., Martín-Navarro, I., & Falcón-Barroso, J. 2023, *MNRAS*, 518, 6325
- Sheth, R. K., & Tormen, G. 2004, *MNRAS*, 350, 1385
- Shull, J. M., Smith, B. D., & Danforth, C. W. 2012, *ApJ*, 759, 23
- Simha, S., Burchett, J. N., Prochaska, J. X., et al. 2020, *ApJ*, 901, 134
- Singh, A., Mahajan, S., & Bagla, J. S. 2020, *MNRAS*, 497, 2265
- Sobral, D., van der Wel, A., Bezanson, R., et al. 2022, *ApJ*, 926, 117
- Somerville, R. S., & Davé, R. 2015, *ARA&A*, 53, 51
- Song, H., Laigle, C., Hwang, H. S., et al. 2021, *MNRAS*, 501, 4635
- Sousbie, T. 2011, *MNRAS*, 414, 350
- Sousbie, T., Pichon, C., & Kawahara, H. 2011, *MNRAS*, 414, 384
- Springel, V. 2010, *MNRAS*, 401, 791
- Springel, V., White, S. D. M., Tormen, G., & Kauffmann, G. 2001, *MNRAS*, 328, 726
- Springel, V., White, S. D. M., Jenkins, A., et al. 2005, *Nature*, 435, 629
- Stark, D. V., Kannappan, S. J., Eckert, K. D., et al. 2016, *ApJ*, 832, 126

- Stevens, A. R. H., Diemer, B., Lagos, C. d. P., et al. 2019, *MNRAS*, **483**, 5334
- Stoughton, C., Lupton, R. H., Bernardi, M., et al. 2002, *AJ*, **123**, 485
- Strauss, M. A., Weinberg, D. H., Lupton, R. H., et al. 2002, *AJ*, **124**, 1810–1824
- Takada, M., Ellis, R. S., Chiba, M., et al. 2014, *PASJ*, **66**, R1
- Tempel, E., Stoica, R. S., Martínez, V. J., et al. 2014, *MNRAS*, **438**, 3465
- Tempel, E., Stoica, R. S., & Saar, E. 2013, *MNRAS*, **428**, 1827
- Tero, A., Takagi, S., Saigusa, T., et al. 2010, *Science*, **327**, 439
- Terrazas, B. A., Bell, E. F., Pillepich, A., et al. 2020, *MNRAS*, **493**, 1888
- Teyssier, R. 2002, *A&A*, **385**, 337
- Tonnesen, S., Bryan, G. L., & van Gorkom, J. H. 2007, *ApJ*, **671**, 1434
- Tremmel, M., Karcher, M., Governato, F., et al. 2017, *MNRAS*, **470**, 1121
- Tudorache, M. N., Jarvis, M. J., Heywood, I., et al. 2022, *MNRAS*, **513**, 2168
- Tumlinson, J., Peebles, M. S., & Werk, J. K. 2017, *ARA&A*, **55**, 389
- van de Weygaert, R., & Schaap, W. 2009, in *Data Analysis in Cosmology*, ed. V. J. Martínez, E. Saar, E. Martínez-González, & M. J. Pons-Bordería, Vol. 665, 291–413
- Voit, G. M., Donahue, M., Bryan, G. L., & McDonald, M. 2015, *Nature*, **519**, 203
- Vulcani, B., Poggianti, B. M., Moretti, A., et al. 2019, *MNRAS*, **487**, 2278
- Walker, S., Simionescu, A., Nagai, D., et al. 2019, *SSRv*, **215**, 7
- Wang, K., Avestruz, C., Guo, H., Wang, W., & Wang, P. 2023, *arXiv e-prints*, [arXiv:2309.15306](https://arxiv.org/abs/2309.15306)
- Wang, Y., Zhai, Z., Alavi, A., et al. 2022, *ApJ*, **928**, 1
- Wechsler, R. H., & Tinker, J. L. 2018, *ARA&A*, **56**, 435
- Welker, C., Bland-Hawthorn, J., van de Sande, J., et al. 2020, *MNRAS*, **491**, 2864
- White, S. D. M., Frenk, C. S., Davis, M., & Efstathiou, G. 1987, *ApJ*, **313**, 505
- Wilde, M. C., Elek, O., Burchett, J. N., et al. 2023, *arXiv e-prints*, [arXiv:2301.02719](https://arxiv.org/abs/2301.02719)
- Winkel, N., Pasquali, A., Kraljic, K., et al. 2021, *MNRAS*, **505**, 4920
- Woo, J., Dekel, A., Faber, S. M., et al. 2013, *MNRAS*, **428**, 3306
- Xu, W., Guo, Q., Zheng, H., et al. 2020, *MNRAS*, **498**, 1839
- Yang, X., Mo, H. J., van den Bosch, F. C., Zhang, Y., & Han, J. 2012, *ApJ*, **752**, 41
- Zakharova, D., Vulcani, B., De Lucia, G., et al. 2023, *MNRAS*, **525**, 4079
- Zavala, J. A., Casey, C. M., Scoville, N., et al. 2019, *ApJ*, **887**, 183
- Zhang, B., Lee, K.-G., Krolewski, A., et al. 2023, *ApJ*, **954**, 49
- Zhu, W., Zhang, F., & Feng, L.-L. 2022, *ApJ*, **924**, 132
- Zinger, E., Dekel, A., Kravtsov, A. V., & Nagai, D. 2018, *MNRAS*, **475**, 3654
- Zinger, E., Pillepich, A., Nelson, D., et al. 2020, *MNRAS*, **499**, 768
- Zu, Y., & Mandelbaum, R. 2016, *MNRAS*, **457**, 4360